

Alma Mater Studiorum Università di Bologna  
Archivio istituzionale della ricerca

Patterns of geochemical variability across weakly developed paleosol profiles and their role as regional stratigraphic markers (Upper Pleistocene, Po Plain)

This is the final peer-reviewed author's accepted manuscript (postprint) of the following publication:

*Published Version:*

Amorosi A., Bruno L., Campo B., Di Martino A., Sammartino I. (2021). Patterns of geochemical variability across weakly developed paleosol profiles and their role as regional stratigraphic markers (Upper Pleistocene, Po Plain). *PALAEOGEOGRAPHY PALAEOCLIMATOLOGY PALAEOECOLOGY*, 574, 1-13 [10.1016/j.palaeo.2021.110413].

*Availability:*

This version is available at: <https://hdl.handle.net/11585/871198> since: 2022-02-27

*Published:*

DOI: <http://doi.org/10.1016/j.palaeo.2021.110413>

*Terms of use:*

Some rights reserved. The terms and conditions for the reuse of this version of the manuscript are specified in the publishing policy. For all terms of use and more information see the publisher's website.

This item was downloaded from IRIS Università di Bologna (<https://cris.unibo.it/>).  
When citing, please refer to the published version.

(Article begins on next page)

This is the final peer-reviewed accepted manuscript of:

Amorosi A.; Bruno L.; Campo B.; Di Martino A.; Sammartino I.: *Patterns of geochemical variability across weakly developed paleosol profiles and their role as regional stratigraphic markers (Upper Pleistocene, Po Plain)*

PALAEOGEOGRAPHY PALAEOCLIMATOLOGY PALAEOECOLOGY VOL. 574 ISSN 0031-0182

DOI: 10.1016/j.palaeo.2021.110413

The final published version is available online at:

<https://dx.doi.org/10.1016/j.palaeo.2021.110413>

Terms of use:

Some rights reserved. The terms and conditions for the reuse of this version of the manuscript are specified in the publishing policy. For all terms of use and more information see the publisher's website.

This item was downloaded from IRIS Università di Bologna (<https://cris.unibo.it/>)

**When citing, please refer to the published version.**

# Patterns of geochemical variability across weakly developed paleosol profiles and their role as regional stratigraphic markers (Upper Pleistocene, Po Plain)

Alessandro Amorosi<sup>1\*</sup>, Luigi Bruno<sup>2</sup>, Bruno Campo<sup>1</sup>, Andrea Di Martino<sup>1</sup>, Irene Sammartino<sup>3</sup>

<sup>1</sup>Department of Biological, Geological and Environmental Sciences, University of Bologna, Italy.

E-mail: [alessandro.amorosi@unibo.it](mailto:alessandro.amorosi@unibo.it), [bruno.campo@unibo.it](mailto:bruno.campo@unibo.it), [andrea.dimartino4@unibo.it](mailto:andrea.dimartino4@unibo.it)

<sup>2</sup>Department of Chemical and Geological Sciences, University of Modena and Reggio Emilia, Italy.

E-mail: [luigi.bruno@unimore.it](mailto:luigi.bruno@unimore.it)

<sup>3</sup>Geologic consultant, Bologna, Italy. E-mail: [Irene.sammartino@gmail.com](mailto:Irene.sammartino@gmail.com)

\*Corresponding author

## Abstract

Weakly developed paleosols from two distinct interfluve surfaces of Late Pleistocene age provide excellent keys to high-resolution stratigraphic correlation and may serve to trace large-scale genetic packages (systems tract equivalents) across the continental portion of the Po Basin. Twenty-four paleosol profiles from 17 sediment cores were identified and characterized for bulk-geochemical analysis. X-ray fluorescence data were used to trace the degree of weathering. Paleosols, 0.5-1.5 m thick, are pedogenically altered floodplain deposits, developed over time spans of a few thousand of years and mostly partitioned into A-Bk horizons. The most notable paleosol features are dark, organic-matter-rich and carbonate-free mineral surface horizons (A) that overlie bright calcic horizons (Bk) typified by the accumulation of secondary carbonates in the form of pedogenic nodules.

Paleosol profiles exhibit a homogeneous geochemical signature that fingerprints a moderate degree of weathering, with little strike- and dip-oriented variability across the different study localities. Plots of Al-normalized calcification and base loss indices against depth reveal systematic increasing values from intensely altered A horizons to underlying Bk horizons. These trends reflect consistent patterns of Ca translocation from surface horizons deeper into the profile, with significant to almost complete Ca removal from A horizons through leaching and accumulation in Bk horizons. Selected trace element ratios (Ba/Sr, Rb/Sr), redox-sensitive trace elements and Zr contents display opposite, up-profile increasing trends that reflect Sr loss in A horizons, with selective Zr concentration in residual minerals.

Vertical trends in element ratios are laterally extensive and consistent on a regional basis and represent key pedochemical/stratigraphic markers that can be traced over great distances (tens of

kms) throughout the inland portion of the basin. Through quantitative assessment of the degree of weathering, geochemical profiling provides high potential for robust subsurface paleosol correlation that might not be captured by visual core descriptions alone.

Keywords: Paleosol stratigraphy; Paleosol maturity; Interfluvial; Sequence stratigraphy; Sequence boundary; Geochemistry

## 1. Introduction

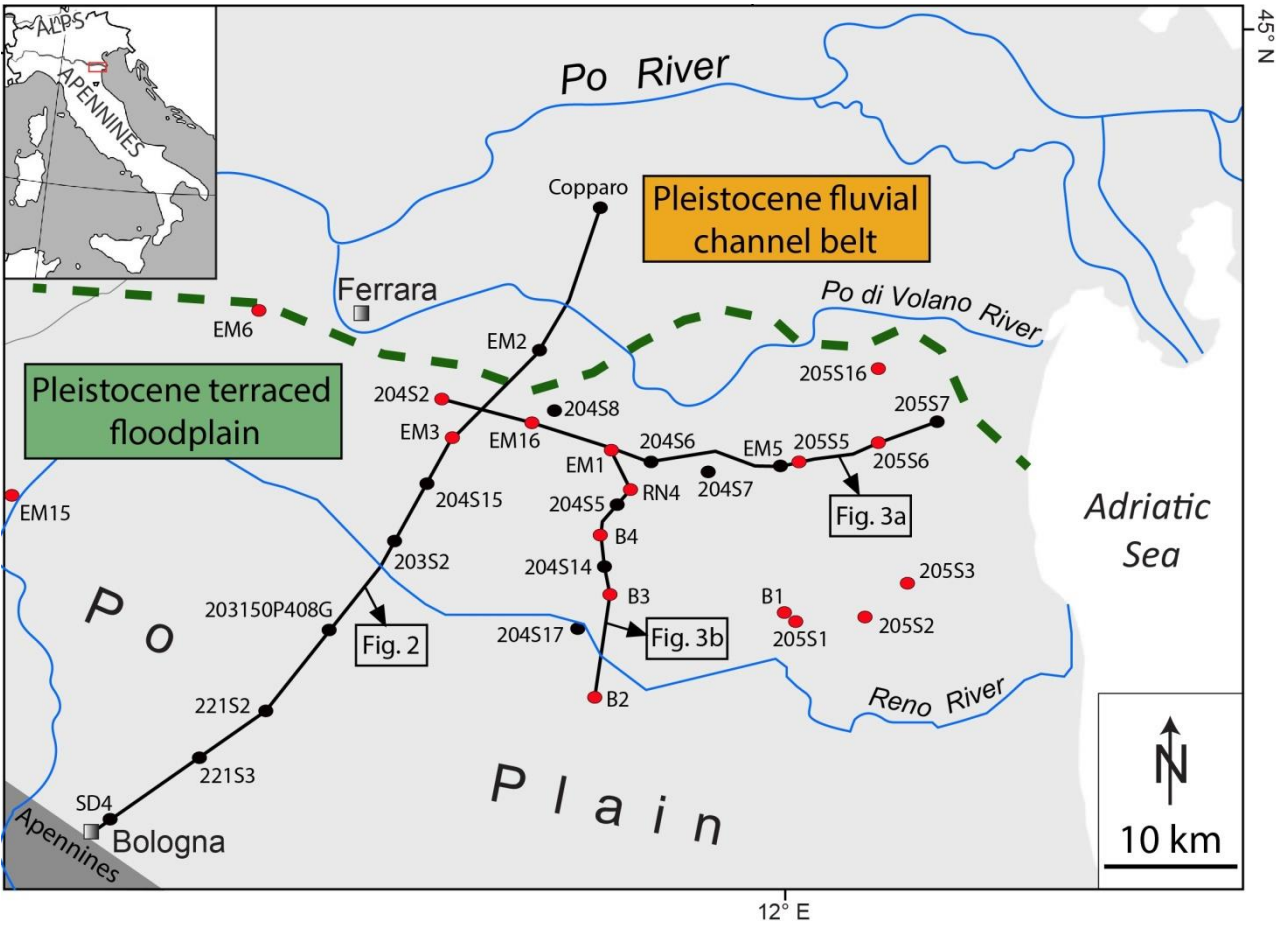
Paleosol-bearing alluvial successions contain a hierarchical record of cyclic sediment accumulation produced in response to the combined effect of autogenic and allogenic controlling mechanisms (Cleveland et al., 2007). Paleosols at sequence-bounding unconformities, in particular, may serve as useful regional stratigraphic markers to trace genetic packages across the basin and to determine regional accommodation trends (Demko et al., 2004).

According to sequence-stratigraphic models, paleosol units commonly correlate with incision along the major drainage axes (Van Wagoner et al., 1990) and well-developed, mature interfluvial paleosols correlate to valley-floor erosion surfaces (Gibling and Bird, 1994; Aitken and Flint, 1996; Shanley and McCabe, 1994; McCarthy and Plint, 1998; 2003; Plint et al., 2001; Atchley et al., 2004; Blum and Aslan, 2006; Cleveland et al., 2007; Srivastava et al., 2010; Raigemborn and Beilinson, 2020).

Models of paleovalley architecture and paleosol-valley relations have been evaluated using Quaternary examples, where proxy records are well established for climate and sea level and periods of incision and aggradation can generate discontinuity-bounded sequences on timescales as short as  $10^3$  to  $10^4$  years (Gibling et al., 2011). In such examples, valley fills are less distinctive and their bases do not correspond to prominent paleosols. Stacked weakly developed paleosols may form terrestrial condensed sections that record prolonged periods of minimal sedimentation in interfluvial position (Gibling et al., 2011; McCarthy and Plint, 2013).

Vertical successions of poorly mature paleosols have been widely described from the Upper Pleistocene subsurface record of the Po Plain, in Italy (Amorosi et al., 2017b; Bruno et al., 2018). Stiff, pedogenized floodplain silts and clays are widely preserved south of the modern Po River and

67 correlate in the north to genetically-related fluvial facies, where thick channel-belt sand bodies  
 68 represent the dominant subsurface stratigraphic unit (Fig. 1).  
 69



70  
 71 *Fig. 1. Location map of studied cores (red dots), with indication of the boundary between the*  
 72 *buried Pleistocene (pre-LGM) terraced floodplain and the coeval fluvial channel-belt sand bodies*  
 73 *(green dashed line, from Morelli et al., 2017). Section trace of Figure 2, transects in Fig. 3, and*  
 74 *location of additional cores used for stratigraphic correlation (black dots) are also shown.*  
 75

76 The Upper Pleistocene-Holocene sedimentary succession provides a particularly well-  
 77 established temporal framework, founded largely on  $^{14}\text{C}$  data, within which immature paleosols  
 78 delineate time-equivalent stratal surfaces and represent key stratigraphic markers that can be  
 79 traced on a regional scale. Three paleosols of Late Pleistocene age (P1-P3) and a younger paleosol  
 80 marking the Pleistocene-Holocene boundary (PH) were recognized for the first time from core  
 81 analysis in the Bologna area (Amorosi et al., 2014a). Subsequent studies examined the basin-scale  
 82 distribution of these paleosols (Amorosi et al., 2017b; Bruno et al., 2019) and their likely climatic  
 83 significance (Bruno et al., 2020). Morelli et al. (2017) carried out the detailed subsurface mapping  
 84 of the youngest two paleosols: paleosol P3, formed at the onset of the Last Glacial Maximum

(LGM), and paleosol PH, encompassing the Younger Dryas (YD) cold event, which marked the short-lived return to glacial conditions after the Late Glacial Interstadial. Although upper Quaternary paleosols clearly exhibit a high potential for regional correlations, only reconnaissance geologic investigation has been undertaken and no detailed paleosol characterization has been attempted, so far.

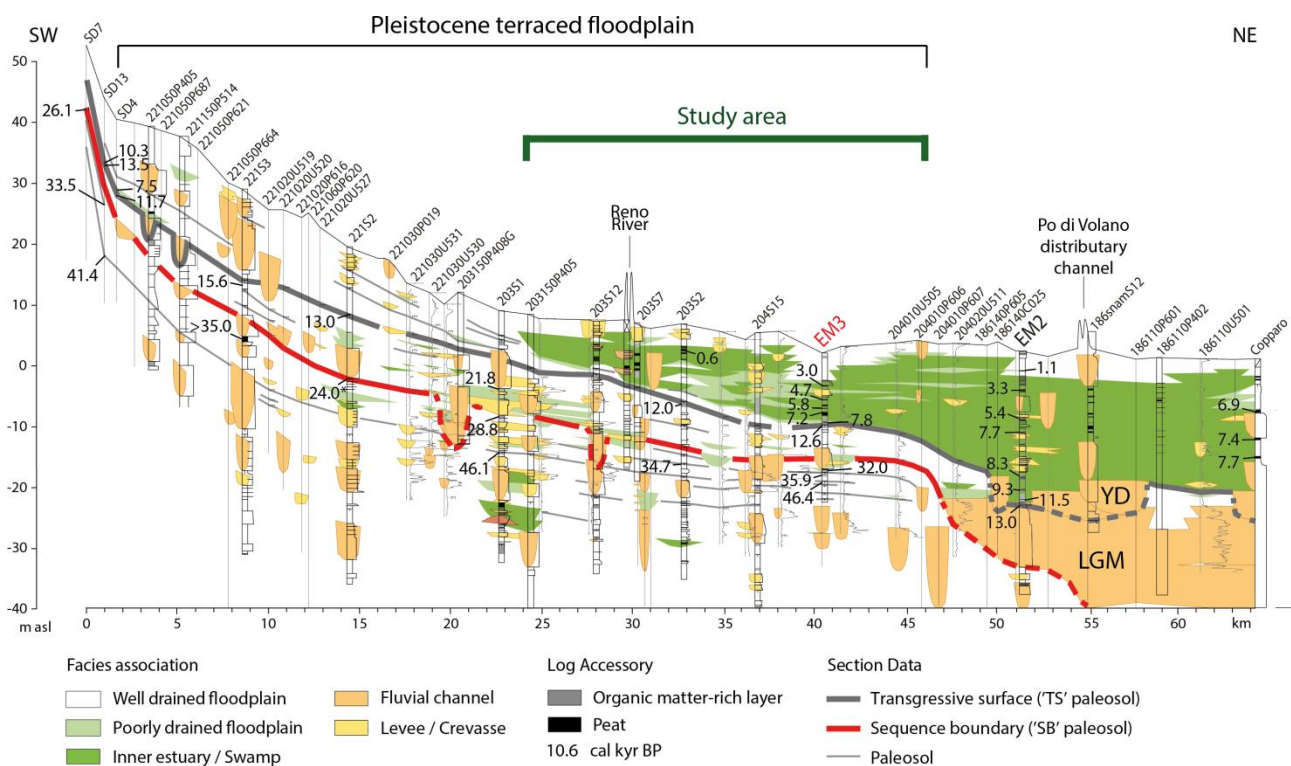
In this study, a comprehensive geochemical investigation of paleosols P3 (LGM paleosol) and PH (YD paleosol) was performed for the first time. The aim of this paper is to provide quantitative assessment of paleosol maturity across these two pedogenized key stratigraphic surfaces, which in a sequence-stratigraphic perspective coincide with the sequence boundary (SB) and the landward equivalent of the transgressive surface (TS), respectively (Fig. 2). Specific objective is to document the stratigraphic utility of immature paleosols for regional correlations within a chronologically constrained sequence-stratigraphic framework. Below the Holocene succession, the study area reveals a wide, buried Late Pleistocene interfluvial belt between the Apennines margin and the coeval fluvial channel-belt bodies in the modern Po River area (Fig. 1). Age-equivalent strata successions are compared from 17 sediment cores, approximately 80 km apart. This study incorporates high-resolution stratigraphic data, paleosol descriptions and geochemistry.

## **2. Stratigraphic overview**

Previous work provides a solid foundation of the shallow subsurface stratigraphy of late Quaternary continental deposits in the Po Plain (Amorosi et al., 2014a; 2017b; Morelli et al., 2017; Bruno et al., 2018; 2020). In this rapidly subsiding setting with high rates of sedimentation, no persistent incised valley was established during the last interglacial/glacial transition and aggradationally-stacked, shallow-incised fluvial bodies are laterally associated with overbank packages, a few m thick, bounded by poorly mature paleosols (Amorosi et al., 2017b – Fig. 2). These paleosols, which define large-scale, though shallow degradation across the Po Plain interfluvial belt, associated to short (2-5 kyr) gaps in sedimentation document widespread, but short-lived, subaerial weathering across poorly dissected, interfluvial areas (Amorosi et al., 2017b; Bruno et al., 2020).

A hierarchy of Upper Pleistocene paleosols has been identified and framed through high-resolution sequence stratigraphic analysis within a strongly constrained chronological setting,

117 founded on tens of radiocarbon dates (Fig. 2). Two prominent paleosols, in particular, exhibit very  
 118 high lateral continuity on a regional scale and are genetically related to fluvial channel-belt sand  
 119 bodies identified to the north, beneath the modern Po River (Morelli et al., 2017 – Fig. 2).  
 120 Paleosol-bounded overbank intervals have sequence-stratigraphic significance within the LGM  
 121 depositional sequence and represent low-accommodation deposits. Based on detailed  
 122 stratigraphic correlation with coeval littoral and shallow-marine facies associations, the two  
 123 paleosols (paleosols P3 and PH of Amorosi et al., 2014) have been interpreted to represent the  
 124 sequence boundary (SB) and the landward equivalent of the transgressive surface (TS),  
 125 respectively (Amorosi et al., 2017a – Fig. 2).  
 126



127  
 128 *Fig. 2. Regional stratigraphic cross-section (section trace in Fig. 1) showing relationship of*  
 129 *floodplain paleosols to their contemporaneous fluvial channel-belt sand bodies (modified after*  
 130 *Amorosi et al., 2017b). Weakly-developed paleosols are typically arranged in thin, paleosol-*  
 131 *bounded overbank sequences and are associated to larger trunk channels amalgamated into*  
 132 *multilateral channel belts. The paleosol at the sequence boundary ('SB' paleosol) was generated at*  
 133 *the MIS 3/2 transition and correlates to fluvial channel-belt bodies assigned to the Last Glacial*  
 134 *Maximum (LGM). The landward equivalent of the transgressive surface ('TS' paleosol) marks the*  
 135 *Pleistocene-Holocene boundary and correlates to Younger Dryas (YD) channel belts.*  
 136  
 137

138 Sea-level lowering and climate-driven forcing have been invoked to account for shallow incision  
 139 and coeval soil development in the Po Plain during the latest Pleistocene (Amorosi et al., 2017b;

140 Bruno et al., 2018; 2020). Pedogenic modification of floodplain silts and clays occurred at the MIS  
141 (Marine Isotope Stage) 3/2 transition, between 30 and 24 cal kyr B.P. (SB paleosol), and during the  
142 protracted sea-level lowstand, when fluvial entrenchment terraced the formerly active (pre-LGM)  
143 alluvial plain, which underwent extensive pedogenic modification. Shallowly-incised tributary  
144 valleys (see Kvale and Archer, 2007) form part of a surficial (Cremaschi, 1987; Castiglioni, 2001;  
145 Bersezio et al., 2007) and subsurface (Bruno et al., 2017b, 2018; Morelli et al., 2017) mappable  
146 drainage network feeding into the much larger Po fluvial system.

147 The SB interfluvial paleosol caps a series of weakly expressed profiles that reflect multiple-step  
148 pedogenic history mostly occurring during MIS 3 (Bruno et al., 2020). Individual paleosols are  
149 generally stacked and separated by thin layers of overbank material (compound paleosols of  
150 Marriott and Wright, 1993). However, they may locally display overlapping profiles with A-B  
151 overprinting (composite paleosols) and pedogenic features may extend throughout much of the  
152 stratigraphic section. The SB paleosol correlates to the base of highly lenticular, valley-filling sand  
153 bodies, typically 20 to 30 m thick and 5 to 20 km wide, that display virtually no pedogenesis (Fig.  
154 2).

155 A younger, regionally extensive paleosol (TS paleosol in Fig. 2) correlates with a short-lived  
156 episode of shallow fluvial incision developed around the Pleistocene-Holocene boundary (Amorosi  
157 et al., 2017b). Radiocarbon dates from this paleosol in the study area cluster around the Younger  
158 Dryas cold reversal (Fig. 2). Paleosol TS is simple. In the subsurface of the modern coastal plain it is  
159 invariably overlain by a deepening-upward succession of Holocene swamp, lagoonal, coastal and  
160 shallow-marine deposits and for this reason it is interpreted as the landward equivalent of the TS.

161 Soil formation at the MIS 3/2 transition has been described from other parts of the world. The  
162 primary influence on regional water table lowering at the MIS 3/2 transition was relative sea-level  
163 fall (Blum and Price, 1998; Dabrio et al., 2000; Autin and Aslan, 2001; Anderson et al., 2004;  
164 Busschers et al., 2007; Kasse et al., 2010; Fan et al., 2018). Similar, coeval paleosols have been  
165 reported from the Yangtze River, where compound paleosols (pedocomplexes) resulted from  
166 alternating deposition and pedogenesis on the paleointerfluvial (Chen et al., 2008). Fluvial incision  
167 and soil development around the Pleistocene/Holocene boundary have been recorded in other  
168 European fluvial systems (Mol et al., 1997; van Balen et al., 2010; Janssens et al., 2012).

169  
170  
171  
172



### 3. Methods

Within detailed measured sections from 17 cores (Fig. 1, Supplementary Table 1), 24 soil profiles were investigated and characterized for geochemical composition. Ten paleosols marking the sequence boundary ('SB' paleosols) and 14 younger paleosols formed at the transgressive surface ('TS' paleosols) were studied. The locations of the cores were chosen to provide as extensive coverage as possible across the two terraced paleosurfaces (Morelli et al., 2017). Geochemical analysis was carried out on all the study cores to extract elemental concentrations. A total of 100 soil samples were analyzed (Supplementary Table 2): 62 from 'TS' paleosols and 38 from compound/composite 'SB' paleosols. We also analyzed 11 samples from unaltered floodplain parent material from the same cores. This study is based largely on the stratigraphic distribution of macromorphological features of pedogenesis and on geochemical characterization of paleosols. Micromorphological investigations were not attempted.

Cores, 17 to 52 m thick, were split lengthwise and carefully described for their sedimentological characteristics. Facies analysis was carried out on a centimetre scale. Graphic logs of cores include description of lithology, grain size, primary sedimentary structures, lamination styles, bioturbation levels and accessory components.

Paleosols at key stratigraphic intervals were recognized by visual inspection of core material. Profile descriptions include horizonation, horizon thickness, color, reaction, redoximorphic features, carbonate accumulations, and other standard soil observations. Moist colors of mottles and matrix were described. Composition, size, and abundance of nodules and other mineral segregations were also characterized. Geotechnical properties were obtained through pocket penetration measurements. Horizon designations are based upon core-observed features in the paleosols after Soil Taxonomy (Soil Survey Staff, 1999).

Paleosols were sampled by horizon for bulk chemical analysis. Series of three to six samples were taken per paleosol profile from the top to a maximum depth of 150 cm. Major and trace element geochemistry was determined by X-ray fluorescence spectroscopy (XRF). Cores were analyzed at Bologna laboratories. Samples were oven dried at 50°C, powdered and homogenized in an agate mortar and analyzed using a Philips PW 1480 spectrometer (Philips, Almelo, The Netherlands). The matrix correction methods of Franzini et al. (1972), Leoni and Saitta (1976) and Leoni et al. (1982) were followed.

204 Analytical methods resulted in data for 29 elements: 10 major elements, reported as oxide  
205 percent by weight ( $\text{SiO}_2$ ,  $\text{TiO}_2$ ,  $\text{Al}_2\text{O}_3$ ,  $\text{Fe}_2\text{O}_3$ ,  $\text{MnO}$ ,  $\text{MgO}$ ,  $\text{CaO}$ ,  $\text{Na}_2\text{O}$ ,  $\text{K}_2\text{O}$ , and  $\text{P}_2\text{O}_5$ ), 18 trace  
206 elements (Ba, Ce, Co, Cr, Cu, Ga, La, Nb, Ni, Pb, Rb, S, Sc, Sr, V, Y, Zn, and Zr), and the loss on  
207 ignition (LOI). LOI, evaluated after overnight heating at  $950^\circ\text{C}$  ( $\text{LOI}_{950}$ ), represents a measure of  
208 volatile substances (weight %, wt%), including pore water, inorganic carbon and organic matter.  
209 The XRF analytical protocol reports major elements in oxide weight percent and trace elements in  
210 parts per million. The estimated precision and accuracy for trace element determinations were  
211 better than 5%. For elements with low concentrations ( $<10$  mg/kg), the accuracy was 10%.

212

213

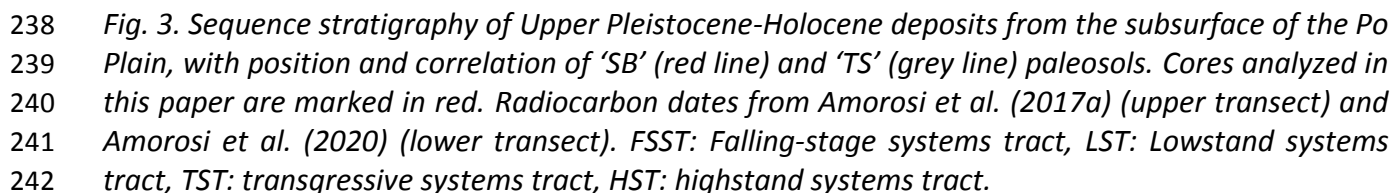
#### 214 **4. Paleosol stratigraphy**

215

216 The Upper Pleistocene-Holocene stratigraphy in the study area was depicted along two  
217 transects, on the basis of stratigraphic and sedimentological data from 18 continuous cores and 36  
218 piezocone (CPTU) penetration tests (Fig. 3). The W-E transect (Fig. 3a) runs roughly in proximal to  
219 distal direction across the buried Pleistocene terraced floodplain, 5-15 km from the southern  
220 margin of the Po paleovalley system, whereas the S-N transect (Fig. 3b) runs perpendicular to the  
221 regional axis of the Northern Apennines (Fig. 1).

222 In this study, we did not focus on facies architecture, which has been the subject of several  
223 published papers and that will not be reiterated here. Summary characteristics of major facies  
224 associations are summarized in Table 1. For detailed description and interpretation of coastal plain  
225 to shallow-marine deposits, the reader is referred to previously published material (Amorosi et al.,  
226 2017a; 2020; Bruno et al., 2017b; 2019; Campo et al., 2020). In this paper, we focused, instead, on  
227 the identification, characterization and tracing of paleosols at two discrete stratigraphic horizons,  
228 corresponding to the SB and TS (Fig. 2). Paleosols identified in cores (Fig. 4) were calibrated against  
229 CPTU tests and tracked laterally based on distinctive changes in log character. The key  
230 geotechnical features to infer paleosols from CPTU tests include: (i) a subtle, but consistent  
231 increase in cone resistance with depth, (ii) a sharp peak in the sleeve friction, recording the sharp  
232 contrast between normally consolidated floodplain facies and underlying stiff, pedogenically  
233 modified deposits, and (iii) an abrupt decrease in pore pressure (Amorosi and Marchi, 1999; Choi  
234 and Kim, 2006; Amorosi et al., 2017b; Bruno et al., 2019).

235



251

252

Facies Association	Lithology Sedimentary structures	Fossils
Fluvial channel	coarse to medium sand, FU trend, high-angle cross-lamination, 2-10 m thick	generally barren
Crevasse/levee	alternating sand and silt, parallel lamination, climbing ripples, 0.5-3 m thick	
Floodplain	clay and silty clay, bioturbation, root traces, mottling, paleosols, 1-20 m thick	generally barren, rare freshwater
Poorly drained floodplain	organic-matter-rich clay, roots, plant remains, 1-5 m thick	rare freshwater
Distributary channel	medium to fine sand, FU trend, high-angle cross-lamination, 2-10 m thick	generally barren, rare freshwater to low brackish
Bay-head delta	medium to fine sand, high-angle cross-lamination, plant debris, 2-5 m thick	mixed freshwater/brackish
Inner estuary/swamp	soft clay, plant debris, wood fragments, peat, parallel lamination, 1-20 m thick	freshwater to low brackish
Outer estuary/lagoon	bioturbated clay, clay-sand alternations, 1-5 m thick	brackish
Delta front/beach barrier	fine to coarse sand, high-angle cross-lamination, parallel lamination, 1-10 m thick	littoral
Prodelta/offshore	organic-matter-rich silty clay, bioturbated clay, 1-7 m thick	marine

*Table 1. Summary characteristics of major lithofacies assemblages in the study area.*

The Holocene succession displays a characteristic retrogradational to aggradational/progradational stacking pattern of facies that defines the transgressive systems tract (TST) and highstand systems tract (HST), respectively (Fig. 3). Holocene deposits rest unconformably on the TS paleosol with typical onlap geometries (Fig. 3a) and provide a detailed understanding of the stratigraphic development of the coastal plain under transgressive and normal regressive conditions. They cover a great diversity of facies associations (Campo et al., 2017) that represent coeval depositional environments, ranging from shallow-marine (offshore and prodelta) through coastal, brackish (outer estuary/lagoon) and freshwater (inner estuary/low-lying swamps).

In the study area, the top surface of the TS paleosol coincides with the landward equivalent of a surface of marine flooding that denotes subsequent transgression (Fig. 3a). Over most of the study area, the overlying Holocene sedimentary succession is dominated by single-story distributary-channel sand bodies encased in organic-rich clays, with a tongue of thin brackish (lagoonal) deposits that demarcate the maximum flooding surface (Fig. 3b). Peat-bearing deposits accumulated in low-lying, permanently waterlogged environments in the inner portion of a transgressive estuary and in the delta plain of a prograding delta system.

There is no dramatic change in depositional style in the two sections of Fig. 3, except for the notable deformation of Quaternary strata in the 204S17-B3 cores area (Fig. 3b), which has been interpreted to reflect recent tectonic activity of the buried anticline structures (Amorosi et al., 2020). Though discontinuous due to local truncation or poor development onto sandy substrates,

277 paleosols on floodplain deposits can be typically traced laterally for about 40 km and appear to  
278 have been developed on a gently inclined slope (Fig. 3).

279

280

## 281 **5. Paleosol description**

282

283 Upper Pleistocene paleosols in the subsurface of the Po Plain are easily differentiated from  
284 overlying and underlying (unaltered) units by their stiff texture and color-banded appearance (Fig.  
285 4). They all are silt- and clay-rich and are typically formed on muddy (floodplain) deposits.

286 Soil profiles typically consist of a dark, organic-rich and bioturbated silt (A horizon) that  
287 gradually overlies a paler horizon (Bk). Paleosol colors are relatively uniform throughout horizons  
288 A and B. Dominant colors are grey to brownish grey and dark brown in horizons A and light grey to  
289 pale yellow in the deeper horizons (Fig. 4).

290 Organic matter imparts the dark color in A horizons. Macroscopic features include root traces,  
291 wood debris, and plant fragments that are scattered throughout the unit. A horizons are barren  
292 with fossils and weakly reactive or unreactive to 10% dilute HCl. Pedogenic carbonate appears  
293 within 30-80 cm of the soil surface (Bk horizon), persisting to depths of about 100-150 cm (Fig. 4).  
294 Calcic horizons (Soil Survey Staff, 1999) can be thick and diffuse or thinner and more concentrated.  
295 Within Bk horizons,  $\text{CaCO}_3$  concretions are visible to the naked eye, generally as pseudomycelia  
296 and few to common hard nodules. Powdery and filamentous carbonate is commonly observed  
297 between nodules. Carbonate nodules are well-rounded to sub-rounded and range from diffuse,  
298 poorly cemented concentrations to discrete, well-cemented masses. Locally, nodules may be  
299 larger than > 1 cm in diameter and may coalesce to form cemented or indurated, thin massive  
300 layers (Bkm).

301 A less common subsurface paleosol horizon that may be associated to the Bk horizon is Bw (Fig.  
302 4). Pedogenized deposits in this case display root traces, local yellow, brown and orange colors  
303 and no carbonates. Black mottles likely derive from different manganese oxide species coating  
304 primary particles.

305

306

307

308

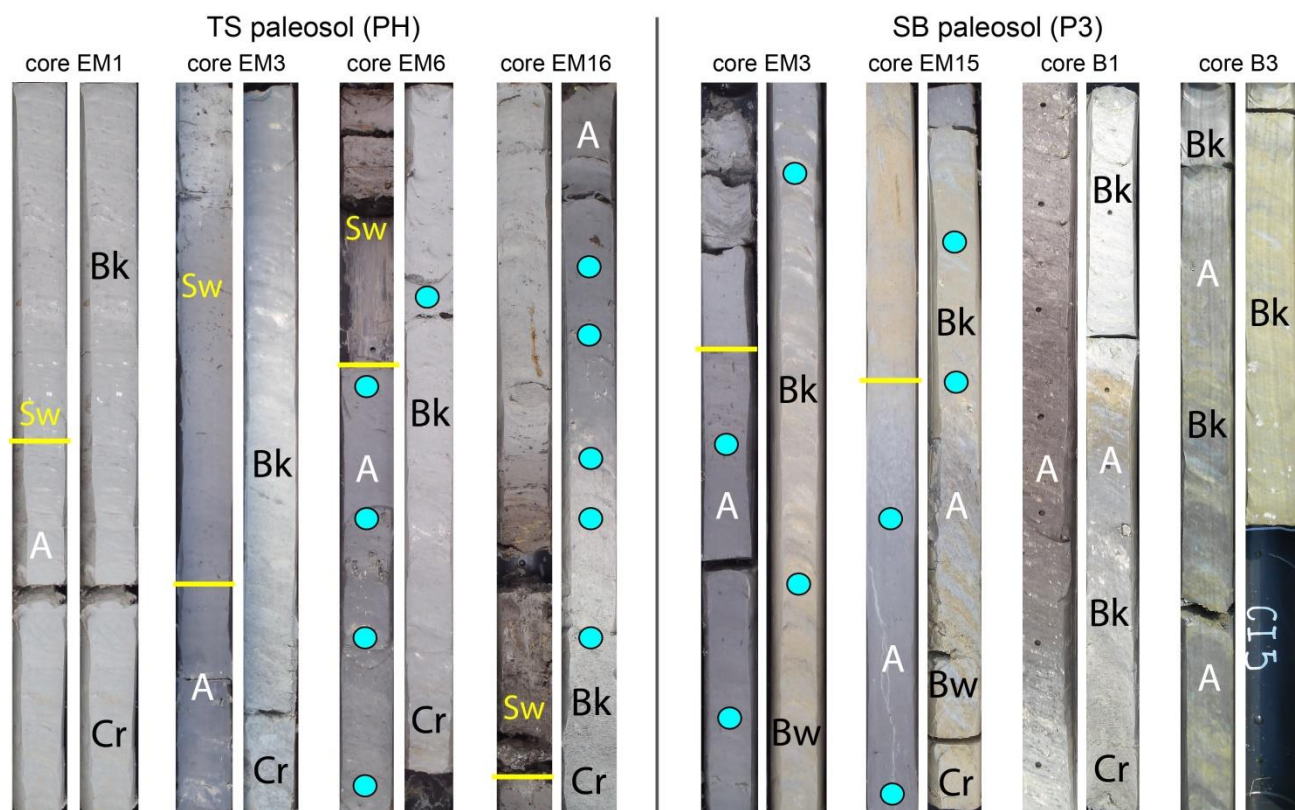


Fig. 4. Representative profiles of paleosols ‘TS’ and ‘SB’ showing A/Bk/Bw/Cr horization (for location, see Fig. 1; paleosol stratigraphy in Fig. 3). TS paleosols are simple A/Bk profiles, invariably overlain by Holocene transgressive deposits (inner estuary/swamp facies association - Sw), suggesting increased waterlogging and flooding in response to a rising water table. Paleosols spanning the sequence boundary (SB) consist of vertically stacked immature paleosols. Light blue dots indicate samples plotted in the geochemical profiles of Fig. 6. Core length is 1 m.

The unweathered (Cr) horizon retains the character of the unconsolidated parent material (floodplain deposits) and as such does not display pedogenic structure or significant rooting. To define the original material, we also determined average bulk compositions of unweathered floodplain sedimentary packages from the same stratigraphic succession.

Paleosols identified in cores also exhibit diagnostic engineering properties (Amorosi et al., 2015), with substantially higher compressive strength coefficients than all other fine-grained, alluvial (floodplain) facies. Specifically, paleosols are typified by distinctive penetration resistance, in the range of 3.5-5 kg/cm<sup>2</sup>, with maximum values in Bk horizons (Amorosi et al., 2015). On the other hand, non-pedogenized floodplain deposits invariably display lower pocket penetration values (average value: 2.0 kg/cm<sup>2</sup>).



## 6. Paleosol geochemistry

Major elements are commonly used to define the net effect of ancient chemical weathering from paleosols (Retallack, 2001). Several oxide ratios have been developed to assist with the interpretation of soil-forming processes in paleosols (Birkeland, 1999; Retallack, 2001). In general, alkali (Na and K) and alkaline earth (Ca and Mg) elements are mobile (Sheldon and Tabor, 2009) and are preferentially released from their host minerals during weathering (Mohanty and Nanda, 2016), whereas the elements Al, Ti and Zr are considered to be chemically immobile in weathering environments.

Several major element indices, such as the Chemical Index of Alteration-CIA,  $\text{Al}_2\text{O}_3/(\text{Al}_2\text{O}_3+\text{CaO}+\text{Na}_2\text{O}+\text{K}_2\text{O})$  (Nesbitt and Young, 1982), the Chemical Weathering Index-CWI,  $\text{Al}_2\text{O}_3/(\text{Al}_2\text{O}_3+\text{CaO}+\text{Na}_2\text{O})$  (Harnois, 1988), or the  $\Sigma\text{Bases}/\text{Al}$  ratio,  $(\text{CaO}+\text{MgO}+\text{Na}_2\text{O}+\text{K}_2\text{O})/\text{Al}_2\text{O}_3$  (Retallack, 1999) provide an indication of leaching of the bases from the soil system in response to weathering intensity, measuring the loss of mobile cations  $\text{Ca}^{2+}$ ,  $\text{Mg}^{2+}$ ,  $\text{Na}^+$  and  $\text{K}^+$ , given as oxides, with respect to stable alumina (Ruxton, 1968; Retallack, 1999; Sheldon and Tabor, 2009). These indices, based on the ratio of a group of highly mobile oxides to one or more immobile oxides, are the best candidates to characterize weathering-induced changes (Price and Velbel, 2003; Varela et al., 2018).

In order to compensate for textural heterogeneity, in general we used elemental ratios over simple single-element measurements (Sheldon and Tabor, 2009). To facilitate interpretation of changes in geochemical composition as a result of soil development, values were also calculated from the unweathered parent material, corresponding to Pleistocene floodplain muds (Table 2).

Among the various chemical indices widely used to estimate weathering, we chose key indicators closely related to pedogenic processes (Retallack, 1997a,b,c; Driese et al., 2000; Sheldon and Tabor, 2009):  $\text{SiO}_2$  for the framework material,  $\text{Al}_2\text{O}_3$  for the clay component, CaO and Sr for the carbonate component, labile oxides for the degree of weathering, Zr for residual minerals. Owing to possible biases due to the overwhelming role of Ca relative to Na and K in the study samples (see values of labile oxides in Table 2), we did not use CIA and CWI as primary indicators of the degree of weathering. We also did not select element ratios that include iron in their formulation, because iron concentrations are a reflection of redox conditions, which may be controlled by modern or ancient groundwater levels and may not be consistent throughout the weathering profile (Harnois, 1988).

Horizon	Surface	SiO <sub>2</sub> (%)	±	TiO <sub>2</sub> (%)	±	Al <sub>2</sub> O <sub>3</sub> (%)	±	Fe <sub>2</sub> O <sub>3</sub> (%)	±	MnO (%)	±	MgO (%)	±	CaO (%)	±	Na <sub>2</sub> O (%)	±	K <sub>2</sub> O (%)	±	P <sub>2</sub> O <sub>5</sub> (%)	±
A	SB	56.50	5.10	0.75	0.08	16.48	1.54	5.72	1.03	0.05	0.02	3.57	0.72	1.78	1.51	1.09	0.22	2.81	0.28	0.11	0.02
	TS	55.11	4.72	0.76	0.08	17.08	1.26	5.98	0.76	0.08	0.04	3.36	0.64	1.54	0.83	0.91	0.30	2.83	0.30	0.10	0.02
Bk	SB	41.25	5.09	0.57	0.08	12.69	1.22	5.68	1.30	0.14	0.04	3.68	0.76	14.10	3.50	0.68	0.18	2.17	0.23	0.10	0.02
	TS	39.77	4.43	0.54	0.08	11.74	1.16	4.81	0.83	0.11	0.03	3.85	0.68	16.49	3.79	0.86	0.73	2.03	0.29	0.10	0.02
Cr		48.71	2.49	0.67	0.05	14.01	1.16	5.92	0.82	0.10	0.04	3.94	0.83	8.59	2.22	0.78	0.13	2.57	0.20	0.11	0.01

Horizon	Surface	LOI (%)	±	Ba (mg/kg)	±	Ce (mg/kg)	±	Co (mg/kg)	±	Cr (mg/kg)	±	Cu (mg/kg)	±	Ga (mg/kg)	±	La (mg/kg)	±	Nb (mg/kg)	±	Ni (mg/kg)	±
A	SB	11.15	6.97	444.54	47.60	80.83	13.19	20.23	5.93	134.04	17.78	38.48	6.53	17.90	4.89	45.38	11.52	15.07	2.91	77.50	12.01
	TS	12.26	3.67	424.72	41.79	85.74	18.31	23.80	8.44	148.49	32.42	41.10	16.96	20.39	5.06	44.48	9.81	17.09	2.43	85.70	14.64
Bk	SB	18.93	3.21	310.56	40.12	58.86	11.15	17.92	6.25	114.11	17.66	35.73	7.73	14.13	4.76	30.20	9.12	11.32	3.06	64.64	6.47
	TS	19.68	2.99	298.73	49.05	55.49	13.50	14.06	5.13	111.34	14.88	31.84	6.70	15.00	3.99	29.93	7.27	12.73	2.48	63.94	6.12
Cr		14.59	1.49	336.55	35.41	59.59	8.67	18.47	4.89	138.11	43.87	39.23	6.89	17.80	1.72	32.68	5.28	14.10	0.92	98.25	41.55

Horizon	Surface	Pb (mg/kg)	±	Rb (mg/kg)	±	S (mg/kg)	±	Sc (mg/kg)	±	Sr (mg/kg)	±	V (mg/kg)	±	Y (mg/kg)	±	Zn (mg/kg)	±	Zr (mg/kg)	±
A	SB	21.03	3.34	136.57	16.29	712.19	1010.04	13.08	4.29	154.32	30.51	121.06	16.62	31.30	3.95	105.66	12.60	194.08	32.00
	TS	21.78	2.89	156.08	18.74	773.26	712.82	15.81	5.81	147.64	22.62	135.84	31.60	33.31	4.61	107.89	15.38	194.16	48.24
Bk	SB	15.19	2.38	89.28	14.24	243.46	164.81	14.63	5.53	342.63	152.41	103.70	15.66	22.23	4.21	83.37	11.77	107.56	22.55
	TS	14.18	3.09	93.54	15.11	520.84	609.23	14.01	6.40	332.30	74.79	93.44	16.58	23.29	3.04	77.58	9.50	121.42	30.09
Cr		17.48	2.34	110.72	17.38	172.73	103.66	13.62	4.18	267.82	53.87	105.51	12.99	25.91	1.85	86.52	8.76	129.54	24.91

Horizon	Surface	(CaO+MgO)/Al <sub>2</sub> O <sub>3</sub>		(CaO+MgO+K <sub>2</sub> O+Na <sub>2</sub> O)/Al <sub>2</sub> O <sub>3</sub>		Ba/Sr		Rb/Sr		Al <sub>2</sub> O <sub>3</sub> /SiO <sub>2</sub>		Al <sub>2</sub> O <sub>3</sub> /TiO <sub>2</sub>	
A	SB	0.33	0.12	0.56	0.12	3.00	0.75	0.91	0.17	0.29	0.02	22.17	2.17
	TS	0.29	0.08	0.51	0.09	2.93	0.45	1.08	0.19	0.31	0.04	22.85	2.91
Bk	SB	1.44	0.48	1.67	0.48	1.05	0.45	0.30	0.09	0.31	0.03	22.43	2.21
	TS	1.77	0.48	2.02	0.49	0.96	0.35	0.30	0.09	0.30	0.03	21.85	2.18
Cr		0.91	0.20	1.15	0.21	1.32	0.35	0.44	0.16	0.29	0.02	21.04	1.53

*Table 2. Summary statistics and major- and trace-element indices for paleosols 'TS' and 'SB' (A and Bk horizons) and for unaltered floodplain parent material (Cr horizon). For quantitative primary data, see Supplementary Table 2.*

Key element ratios were calculated (Table 2) along selected paleosol profiles (Fig. 5) and plotted in binary diagrams (Fig. 6). Table 2 permits a comparison of average values for selected geochemical parameters along the study paleosols. Six geochemical indices are reported below as a function of depth.

### 6.1. Calcification index

The (CaO+MgO)/Al<sub>2</sub>O<sub>3</sub> ratio (calcification index) is a general proxy for pedogenic carbonate (calcite and dolomite) accumulations (Retallack, 2001a, b; 2007; Mohanty and Nanda, 2016). Generally, calcification is associated with processes that occur in dry climates where evaporation exceeds precipitation (Delgado et al., 2019).

In the study samples, the calcification index clearly discriminates between low values in A horizons and moderate values in Bk horizons, with no overlap (Fig. 5, Table 2). CaO is strongly depleted in upper A horizons (average values: 1.78% at the SB, 1.54% at the TS), whereas it is significantly enriched in Bk horizons (average values: 14.10% in SB paleosols, 16.49% in TS paleosols). Unaltered floodplain deposits exhibit intermediate values (8.59%). On the other hand, MgO values are fairly constant across distinct paleosol horizons and very similar to unweathered floodplain silts and clays (Table 2). Calculated (CaO+MgO)/Al<sub>2</sub>O<sub>3</sub> ratios for A horizons are all fairly



low, average values ranging between 0.29 (TS paleosols) and 0.33 (SB paleosols). On the other hand, average values for Bk horizons are in the 1.44 (SB paleosols) – 1.77 (TS paleosols) range and denote marked calcification. The calcification index averages 0.91 in unaltered Cr horizons (Table 2).

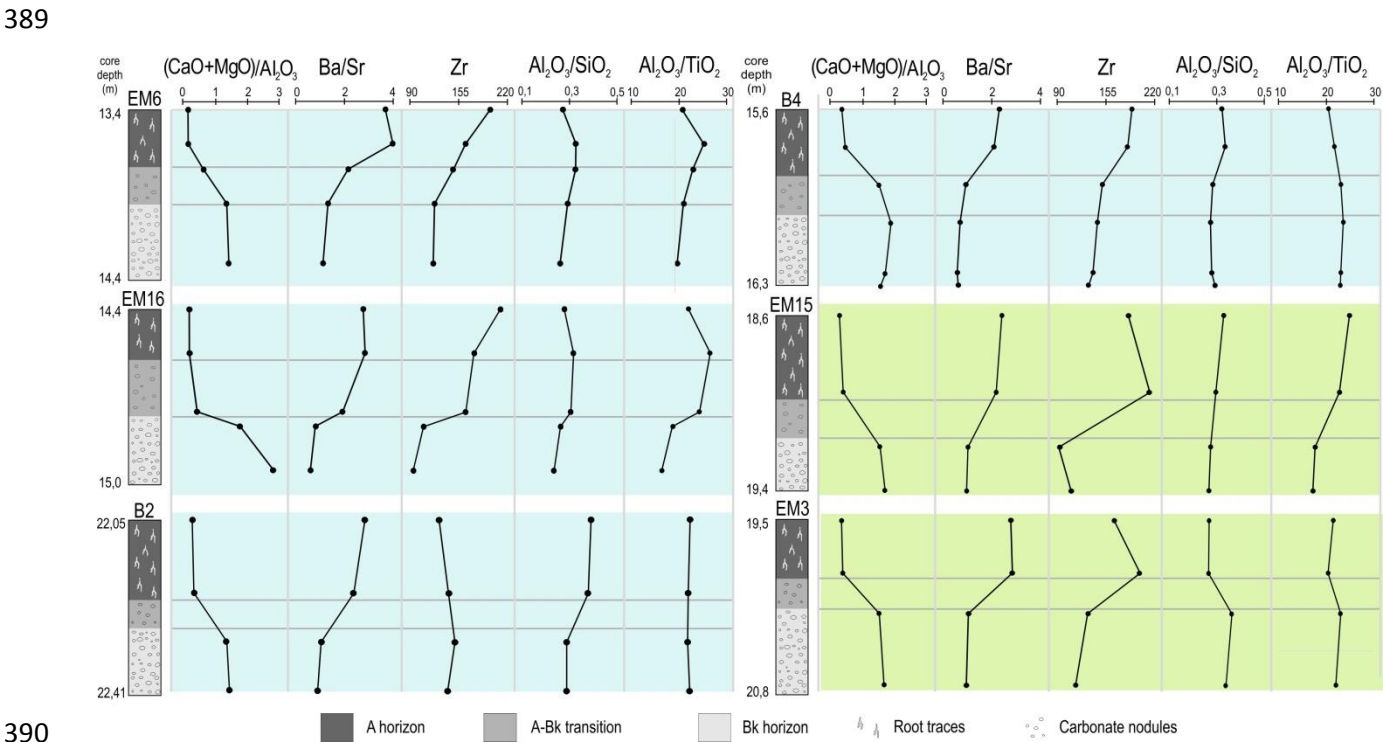


*Fig. 5. Variations of major- and trace-element indices along selected paleosol profiles (see Figs. 3-4). TS paleosols (cores EM6, EM16, B2 and B4) are in light blue, SB paleosols (cores EM15 and EM3) in light green.*

### 6.2. Base loss index

The  $\Sigma\text{Bases}/\text{Al}_2\text{O}_3$  ratio,  $(\text{CaO}+\text{MgO}+\text{Na}_2\text{O}+\text{K}_2\text{O})/\text{Al}_2\text{O}_3$ , measures the loss of mobile cations  $\text{Ca}^{2+}$ ,  $\text{Mg}^{2+}$ ,  $\text{Na}^{+}$  and  $\text{K}^{+}$ , given as oxides, with respect to stable alumina (Ruxton, 1968; Mora and Driese, 1999; Retallack, 1999; Sheldon and Tabor, 2009). This index, which unlike the Chemical Index of Alteration (Nesbitt and Young, 1982) takes into account the role of Mg-bearing minerals, provides an indication of leaching of the bases from the soil system in response to weathering intensity (Retallack, 1999). The  $(\text{CaO}+\text{MgO}+\text{Na}_2\text{O}+\text{K}_2\text{O})/\text{Al}_2\text{O}_3$  index is similar to the Chemical Weathering Index (Harnois, 1988) and is the reciprocal of the hydrolysis ratio (Sheldon and Tabor, 2009). Chemical weathering affects plagioclase preferentially, then K-feldspar (Nesbitt et al., 1996). Calcium, sodium and potassium generally are removed from these minerals by aggressive soil solutions so that the proportion of alkalis to alumina typically decreases in the weathered product (Nesbitt and Young, 1982). In case of overwhelming weathering control, mobile elements are

408 expected to be all depleted in surface horizons (He et al., 2020), whereas Bk horizons typically  
409 exhibit values higher than 1 (Dal' Bó et al., 2009).

410 In Po Plain paleosols, horizons A and Bk are clearly differentiated through the  $\Sigma\text{Bases}/\text{Al}_2\text{O}_3$   
411 ratio (Fig. 6a and Table 2), with notably similar results for older (SB) and younger (TS) paleosols.  
412 Average values for A horizons range between 0.51 (TS paleosols) and 0.56 (SB paleosols), whereas  
413 average values for Bk horizons are in the range of 1.67 (SB paleosols) – 2.02 (TS paleosols). This  
414 index has average value of 1.15 in Cr horizons (Table 2).

415

### 416 6.3. Leaching index

417

418 The Ba/Sr ratio quantifies the amount of leaching during the weathering process using the  
419 behaviour of alkaline earth metals like Ba and Sr (Retallack, 2001a, b; Sheldon and Tabor, 2009;  
420 Scarciglia et al., 2018). Although Ba and Sr have similar atomic radii and the same molecular  
421 affinity, Sr is more soluble than Ba (Vinogradov, 1959) and the Ba/Sr ratio increases with  
422 increasing weathering (Nesbitt and Young, 1982). Strontium dissolution in soils follows the same  
423 pathways as calcium. On the other hand, the chemical behaviour of Ba is less understood than Sr,  
424 particularly in soils (Sheldon and Tabor, 2009). The Rb/Sr ratio has been suggested as another  
425 indicator of the degree of weathering (Chen et al., 1999; Xu et al., 2010). Because the ionic radius  
426 of Rb is close to that of K, Rb generally coexists with K in K-rich minerals, such as K-feldspar and  
427 biotite, whereas Sr is preferentially partitioned into Na- and Ca-bearing minerals, such as  
428 carbonates, plagioclase and amphibole. Weathering can leach Ca and Sr much easier than Rb and  
429 K. As a result, the relict would have higher Rb/Sr ratios compared with the leached fraction. The  
430 Rb/Sr has also been used as a paleoclimatic indicator in loess-paleosol complexes (Chen et al.,  
431 1999).

432 The behaviour of the Ba/Sr leaching proxy mirrors that of the calcification index, allowing  
433 further differentiation between A and Bk horizons (Figs. 5 and 6b). Ba/Sr ratios for A horizons  
434 exhibit moderate average values that range between 2.93 (TS paleosols) and 3.00 (SB paleosols),  
435 whereas consistent, notably lower average values (0.96 for TS paleosols, 1.05 for SB paleosols)  
436 were obtained for Bk horizons. Unaltered floodplain material (Cr horizons) yielded an average  
437 value of 1.32 (Table 2). In the study paleosols, the Rb/Sr ratio behaves as the Ba/Sr ratio and  
438 decreases steadily downcore (Table 2). An obvious trend of Rb enrichment and Sr depletion is  
439 observed in A horizons (Fig. 5). Average values of the Rb/Sr ratio for A horizons range between

0.91 (SB paleosols) and 1.08 (TS paleosols), whereas for Bk horizons they are equal to 0.30. In the parent material (Cr horizon), the Rb/Sr ratio has an average value of 0.44 (Table 2).

#### 6.4. Zr (zirconium)

Trace element geochemistry of paleosols provides valuable information regarding leaching and the degree of weathering (Retallack, 1999; 2001; Kahman et al., 2008; Mohanty and Nanda, 2016). Certain elements, such as Zr and Ti, are preferentially hosted in the densest minerals (e.g., zircon, ilmenite and monazite – Garzanti and Andò, 2019) and their concentration may vary owing to selective-entrainment effects (Garzanti et al., 2013; He et al., 2020). Zirconium (Zr), in particular, is commonly found in minerals that are resistant to alteration and therefore tends to accumulate as weathering progresses (Maynard, 1992; Mongrain et al., 2013; Driese et al., 2000), especially in the very fine sand-silt fraction (Garcia et al., 2003).

In the study paleosols, Zr shows a conspicuous decrease downprofile (Fig. 5 and Table 2), with few exceptions (e.g., core B2). An average value of 194 mg/kg is observed in A horizons, irrespective of paleosol age (SB vs TS), whereas significantly lower average values (108 mg/kg for SB paleosols, 121 mg/kg for TS paleosols) are recorded for Bk horizons. The average Zr concentration for unaltered Cr horizons is 130 mg/kg.

#### 6.5. Clayeyiness index

The  $\text{Al}_2\text{O}_3/\text{SiO}_2$  ratio is a method for quantifying the amount of clay formation (Ruxton, 1968; Retallack et al., 2000; Prochnow et L., 2006), because Al accumulates in clay minerals relative to a silicate parent material (Sheldon and Tabor, 2009). Higher values are indicative of increasing clay formation with the loss of feldspars and other less resistant minerals (Ruxton, 1968; Sheldon and Tabor, 2009).

In the study samples, the clayeyiness index contributes little geochemical signal, with minimal variations across the weathering profiles (Fig. 5), irrespective of paleosol horizons (A versus Bk) or ages (SB versus TS paleosols) (Table 2). For A horizons, average values of the  $\text{Al}_2\text{O}_3/\text{SiO}_2$  ratio are narrowly constrained between 0.29 (SB paleosols) and 0.31 (TS paleosols). B horizons yielded very similar average values, ranging between 0.30 (TS) and 0.31 (SB). A similar clayeyiness average value (0.29) was also obtained for the unweather floodplain material (Cr horizon in Table 2).

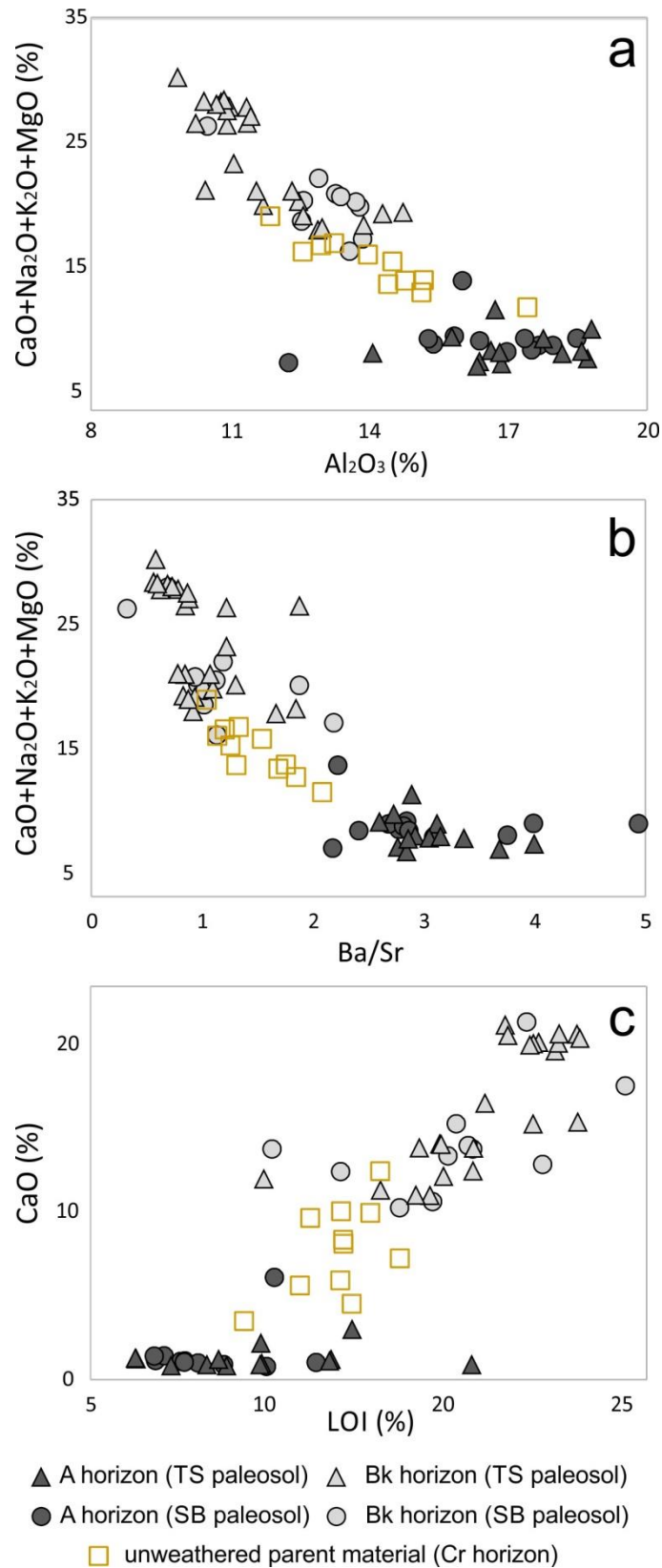


Fig. 6. Geochemical plots for 24 representative paleosols from 17 sediment cores (Fig. 1), grouped by horizon (A versus Bk) and sequence-stratigraphic position ('SB' versus 'TS' paleosols). Data are plotted against geochemical data from unweathered floodplain silts and clays (Cr horizon) from the same cores. a: Cross-plot of  $\text{Al}_2\text{O}_3$  vs  $(\text{CaO}+\text{MgO}+\text{Na}_2\text{O}+\text{K}_2\text{O})$ ; b: Cross-plot of  $\text{Ba}/\text{Sr}$  vs  $(\text{CaO}+\text{MgO}+\text{Na}_2\text{O}+\text{K}_2\text{O})$ ; c: Cross-plot of LOI vs CaO.

479

## 480 6.6. $Al_2O_3/TiO_2$ ratio

481

482 This ratio is particularly useful as a provenance indicator, because Ti contents may be quite  
483 variable among different types of rocks, even as Al contents are relatively constant (Sheldon and  
484 Tabor, 2009). As both Al and Ti are relatively immobile elements, their ratio generally remains  
485 constant during pedogenesis (Delgado et al., 2019).

486 Average ratios of  $Al_2O_3/TiO_2$  exhibit little variation at different profile localities and are fairly  
487 uniform across the various paleosol profiles, with no significant distinction between A horizons  
488 (22.17 for SB paleosols, 22.85 for TS paleosols) and Bk horizons (21.85 for TS paleosols, 22.43 for  
489 SB paleosols). This implies relatively homogeneous provenance.

490 The major geochemical variations shown along six paleosol profiles (Fig. 5) are consistent with  
491 data from 24 paleosols and 17 sediment cores (Fig. 6). In the  $\Sigma Bases/Al_2O_3$  cross-plot (Fig. 6a), data  
492 points from the A horizons, Bk horizons and the unaltered parent material reveal a strong negative  
493 correlation and plot in three distinct clusters, irrespective of the key sequence-stratigraphic  
494 surface (SB or TS) at which sampled were collected. Elemental analysis shows that Bk horizons  
495 invariably have the highest  $CaO+MgO+Na_2O+K_2O$  values. Particularly,  $\Sigma Bases$  yielded higher values  
496 in Bk horizons than in A horizons by an average factor 3.5 (Table 2). Data from the unaltered  
497 parent material invariably fall between these two extremes (Fig. 6a).

498 The roughly linear pattern of the  $\Sigma Bases$  versus  $Al_2O_3$  plot is also seen with some trace  
499 elements, like Ba/Sr (Fig. 6b), and with LOI (Fig. 6c), that behave as CaO. Figures 6b and 6c reveal  
500 that there is a systematic trend in geochemical element distribution, with higher Sr concentrations  
501 and LOI values being prevalent in Bk horizons. At the other extreme, A horizons exhibit the lowest  
502 values in all paleosols.

503

504

## 505 7. Paleosol maturity

506

507 As Upper Pleistocene Po Plain paleosols underwent very incipient diagenesis, they still preserve  
508 most of their morphological and physico-chemical properties and environmental signatures. In  
509 general, paleosols are partitioned into two major pedogenic layers or horizons (Figs. 4-6). Basic  
510 identification features of paleosols include differences in color from darker A horizons to

511 underlying lighter Bk horizons that reflect organic matter inputs in A horizons and calcium  
512 carbonate accumulation in Bk horizons (Schwertmann, 1993).

513 The relative rates of formation and characteristic stages of morphologies of Bk horizons have  
514 been quantified by Gile et al. (1965, 1966), Machette (1985) and Retallack (1988) for modern soils  
515 and Quaternary paleosols. According to such classification schemes, the presence of few to  
516 common carbonate nodules in calcareous (Bk) horizons allows attribution of Po Plain paleosols to  
517 Stage II of carbonate accumulation (Machette, 1985) and to the second stage of paleosol  
518 development (weakly developed paleosols of Retallack, 1988), which in fine-grained materials  
519 imply a few thousands of years to form (Birkeland, 1999). The rates of carbonate dissolution and  
520 reprecipitation in Bk horizons have been modelled by McFadden and Tinsley (1985) and  
521 mathematical models are available to estimate carbonate accumulation in soils (Mc Fadden et al.,  
522 1991; 1998). These studies are consistent with radiometric dating of Po Plain Inceptisols from the  
523 Bologna area, which also concluded that substantial pedogenic carbonate horizons formed during  
524 intervals of time of a few thousand years (Amorosi et al., 2014a; Bruno et al., 2020). Dominance of  
525 pedogenic carbonates in calcic horizons and weak pedogenic development suggest relatively dry  
526 conditions and the presence of a vadose zone and low groundwater table (Demko et al., 2004;  
527 Srivastava et al., 2018; Bruno et al., 2020). The presence of calcareous paleosols at the sequence  
528 boundary and on lowstand surfaces suggests that pedogenesis took place during times of relative  
529 climatic aridity and possibly reduced precipitation (Tandon and Gibling, 1997; Sinha et al., 2007).

530 Examination of geochemistry of Quaternary paleosols yields quantitative estimates of paleosol  
531 maturity and shows that paleosols bracketing the SB or developed at the landward equivalent of  
532 the TS have nearly uniform chemistry and display broadly similar stages of development  
533 throughout both dip-oriented (Fig. 3a) and strike-oriented (Fig. 3b) cross-sections. On  
534 homogeneous parent material, such as in the case of Quaternary Po Plain floodplain deposits,  
535 weathering indices change systematically with depth (Price and Velbel, 2003). Accordingly,  
536 geochemical variations in element ratios are observed at discrete levels within the study paleosols,  
537 allowing the clear differentiation between A and Bk horizons.

538 Pedogenesis may increase the relative amount of alumina in sediments. Nearly constant  
539  $\text{Al}_2\text{O}_3/\text{SiO}_2$  values with depth observed in Po Plain paleosols (Fig. 5 and Table 2) suggest that no  
540 significant clay illuviation took place in deeper horizons. This is consistent with the lack of well  
541 developed argillic (Bt) horizons along the paleosol profiles. Calculated values of the  $\text{Al}_2\text{O}_3/\text{SiO}_2$   
542 ratio are consistent with field observations and indicate that there is little textural variation

543 throughout paleosol profiles. They also indicate that pedogenesis occurred on homogeneous silt-  
544 and clay-rich floodplain facies (Sprague et al., 2009).

545 Degradation of feldspars and other minerals by the removal of base cations (mostly Ca) by  
546 dissolution and concomitant formation of clay minerals is the dominant process during chemical  
547 weathering of silicate rocks (Nesbitt and Young, 1982). Mobile elements hosted in A horizons  
548 undergo extensive leaching and are progressively subtracted from feldspars. Leaching of mobile  
549 components (including CaO and MgO) is associated with enrichment of immobile elements, such  
550 as Zr (Fig. 5 and Table 2).

551 All geochemical proxies behave consistently. Selected indices that are commonly inferred to  
552 quantify the totality of weathering processes, such as calcification and Ba/Sr (Fig. 5 and Table 2)  
553 coherently reflect low degree of weathering under relatively cold climate conditions. It is apparent  
554 that several geochemical elements follow distinct patterns of geochemical variability and that  
555 downcore geochemical trends from all the study cores are consistent along paleosol profiles and  
556 represent pedochemical markers on a basin scale (Delgado et al., 2019). The most notable down-  
557 profile variation is increased concentration of labile oxides (CaO and MgO) with respect to  $Al_2O_3$ .  
558 Such negative Ca translocations from A horizons to underlying Bk horizons largely reflect  
559 weathering and removal of this labile cation relative to stable residual constituents. Base cations  
560 were leached from upper soil horizons in response to acidification processes and rapidly  
561 accumulated within the calcareous subsoil, reflecting the accumulation of pedogenic carbonate.  
562 Elevated LOI values in Bk horizons, paralleled by CaO levels (Fig. 6c), are interpreted to reflect the  
563 liberation of  $CO_2$  during ignition of samples due to abundant carbonate (Cleveland et al., 2008).  
564 LOI data were then not considered further in interpretation.

565 Table 2 outlines the geochemical elements evaluated in this study and provides a comparison  
566 of the six element ratios plotted in Figs. 5 and 6. Significant leaching of the parent material to form  
567 paleosols is also inferred from the Ba/Sr and Rb/Sr ratios, which increase from Bk to A horizons.  
568 The enriched values of these “leaching parameters” in the A horizons are interpreted to reflect Sr  
569 removal from A horizons and accumulation of Sr-rich carbonate nodules in Bk horizons in  
570 association with Ca. Sequestration of Sr in the pedogenic carbonate phases and substitution of Sr  
571 for Ca are likely phenomena in the paleosol profile (Driese et al., 2000).

572 Concentrations of redox-sensitive trace elements, such as Cu, V, Cr, Ni, Co and Zn are notably  
573 higher in A horizons (Table 2). For the other trace elements, Zr is typically enriched in A horizons  
574 (Fig. 5). The abundance of Zr can be controlled by multiple geological factors other than

575 weathering, including parent-rock material, grain size and hydraulic sorting (He et al., 2020). In the  
576 study area, perceptible enrichment in Zr concentration within A horizons is interpreted to reflect  
577 weathering: prolonged stability of interfluvial surfaces is suggested by concentration of resistant  
578 heavy-minerals, such as zircons, in A horizons (Driese et al., 2000; Mongrain et al., 2013).

579

580

## 581 **8. Use of immature paleosols for regional correlations**

582

583 Weakly-developed paleosols represent regional surfaces of non-deposition that play a critical  
584 role in the high-resolution stratigraphy of the Upper Pleistocene, non-marine succession of the Po  
585 Plain. Pedogenic alteration is ubiquitous across the weathered interfluvial surfaces and paleosols in  
586 key stratigraphic positions bear unique and consistent physico-chemical characteristics that can be  
587 effective in delineating subsurface stratigraphy of low-accommodation (FSST+LST) fluvial deposits  
588 on a regional scale (Figs. 2 and 3). Radiocarbon dating of SB and TS paleosols provides values  
589 consistent with radiocarbon ages observed from their updip equivalents, in the Bologna region  
590 (Amorosi et al., 2014a; Bruno et al., 2020). The remarkably similar stratigraphic architecture of  
591 Upper Pleistocene alluvial deposits in the study area (Fig. 3) with respect to regional paleosol  
592 stratigraphy (Fig. 2) suggests a similar history of deposition and pedogenesis that was likely  
593 produced under relatively cold climate conditions (LGM and YD, respectively) in response to  
594 allogenic controlling factors.

595 McCarthy and Plint (2013) have shown that paleosols characteristics at key sequence-  
596 stratigraphic surfaces may vary on a basin scale depending upon their paleo-landscape position  
597 with respect to valley margins and the marine shoreline, and that they can be partitioned into  
598 three distinct spatial zones based on their degree of development and architecture. The study area  
599 (Fig. 1) represents a relatively short segment of the wider Po Plain-Adriatic Sea source-to-sink  
600 system and displays no remarkable lateral variability in terms of physiographic location (Fig. 2).  
601 Within this relatively homogeneous alluvial plain segment, paleosol maturity does not exhibit  
602 significant differences in terms of pedogenic features (Fig. 4) and geochemical properties (Figs. 5-  
603 6). Poor lateral geochemical variability of paleosol characteristics on a km-scale has also been  
604 documented by Driese and Ashley (2016) and by Hyland and Sheldon (2016).

605 Further updip, at a greater distance from the margin of the Po paleovalley system, Late  
606 Pleistocene interfluvial surfaces experienced higher intensities of pedogenic processes owing to



607 their more elevated paleo-landscape position. At these locations, the immature paleosols  
608 (Inceptisols) described from the subsurface of the Po Plain are replaced by an intensely rubified  
609 Alfisol characterized by strong clay illuviation (Cremaschi, 1987; Cremaschi et al., 1990). This soil  
610 crops out continuously at the Apennines foothills and documents through a catenary effect a  
611 remarkably higher degree of soil development than in the buried distal units (Cremaschi and  
612 Nicosia, 2012). For a detailed documentation of alternating phases of sediment aggradation,  
613 stabilization and pedogenesis at the Apennines margin during the Late Pleistocene, the reader is  
614 referred to Zuffetti et al. (2018).

615 Subsurface control may predict the approximate position of SB and TS paleosols across the Po  
616 Basin fill through integration of physical stratigraphy with radiometric data (Figs. 3 and 4). This  
617 study has shown that framing precisely paleosol location into three-dimensional analysis can be  
618 largely aided by intrinsic geochemical properties (Figs. 5 and 6). Paleosol TS, developed at the  
619 Pleistocene/Holocene boundary, is readily recognized by its diagnostic stratigraphic position below  
620 Holocene transgressive deposits (Fig. 3). On the other hand, immature paleosols capped by the SB  
621 may stack one on another in a welded fashion as accommodation lessens (Figs. 2 and 4). For such  
622 paleosols, especially if no radiocarbon dates are available, correlation of soil-forming intervals  
623 bracketing the sequence boundary can be more useful than is attempting to correlate individual  
624 paleosols (McCarthy and Plint, 2013).

625 Extracting the weathering signal from geochemical data is not straightforward, as: (i) bulk  
626 sediment analysis cannot differentiate precisely among the several possible sources of each  
627 element (He et al., 2020); (ii) weathering indices might represent the integrated weathering  
628 history in the river basin, rather than being reliable proxies of instantaneous chemical weathering  
629 (Shao and Yang, 2012); (iii) the geochemistry of sediments can be affected by multiple controls  
630 other than climate-induced weathering, including source-rock lithology (Kraus, 2002) and  
631 hydraulic sorting (Garzanti and Resentini, 2016).

632 A careful evaluation of these diverse controls on sediment composition is possible in the study  
633 area and this can facilitate interpretation of weathering indices as reflecting true weathering  
634 indicators. For example, it is apparent that changes in source-rock lithology did not play a major  
635 role in controlling geochemical signatures of Upper Pleistocene paleosols. Sediment provenance  
636 analysis in the Po Plain based on integrated sand petrography (Tentori et al., 2021) and bulk-  
637 sediment geochemistry (Amorosi et al., 2012, 2014b; Amorosi and Sammartino, 2018; Bruno et al.,  
638 2017b) has shown that overbank parent material reflects a relatively homogeneous (Apennines)

639 source-rock domain for Pleistocene alluvial deposits, as opposed to a remarkably more complex  
640 sediment dispersal pattern developed at the onset of the Holocene (Amorosi and Sammartino,  
641 2018). Size sorting during transportation and deposition generally results in some degree of  
642 mineralogical differentiation, which may modify weathering indices (Garzanti and Resentini,  
643 2016). Restricting paleosol composition to uniform mud grades, as also indicated by remarkably  
644 constant  $\text{Al}_2\text{O}_3/\text{SiO}_2$  ratios (Table 2), makes the influence of grain size on composition minimal  
645 (Nesbitt and Young, 1982). Therefore, the composition of muds will primarily reflect the degree of  
646 weathering.

647 In summary, weathered horizons of Late Pleistocene age bear distinctive geochemical  
648 properties that are laterally traceable for tens of kilometers (Figs. 5 and 6) and that can be used as  
649 highly effective stratigraphic markers across the non-marine portion of the Po Basin fill. They also  
650 represent the key to unravel the sequence-stratigraphic architecture of the non-marine  
651 succession, tracing systems tract boundaries from the downstream segments of the source-to-sink  
652 system into the upstream alluvium.

653

654

## 655 **9. Conclusions**

656

657 Two weakly developed paleosols marking the sequence boundary (SB) and the lateral  
658 equivalent of the transgressive surface (TS), respectively, in the Last Glacial Maximum depositional  
659 sequence are laterally continuous and traceable for tens of kilometers across the non-marine  
660 portion of the Po Basin. Such surfaces provide a comprehensive, three-dimensional view of the  
661 pedogenic character of Late Pleistocene interfluvies. This paper has investigated the modifications  
662 induced by chemical weathering on such pedogenically altered floodplain deposits, focusing on  
663 the recognition, correlation, and characterization of Inceptisol-like paleosols.

664 A comparison of the paleosols, their distribution, and degree of pedogenic development  
665 suggest widespread soil development on short-lived, interfluvial areas. Weakly developed  
666 paleosols mark regional unconformities and contain excellent records of the Late Pleistocene  
667 depositional history. They are linked to minimal incision and their alternation with overbank  
668 deposits into paleosol-bearing cycles reflects conditions of limited accommodation on the  
669 floodplain and their formation as a result of alternate aggradation and degradation. The most  
670 distinctive feature of SB and TS paleosols is soil partitioning into a well identifiable dark, organic-

671 matter-rich and carbonate-free upper A horizon and a lower Bk horizon, typified by the abundance  
672 of calcium carbonate nodules.

673 Weathering patterns, expressed as geochemical trends, of paleosols represent discernible  
674 regional features that define a robust correlation scheme, with small lateral variability and suggest  
675 that floodplain environments were affected by mild, but laterally extensive weathering conditions.  
676 Element ratios used as tracers of the degree of weathering (calcification and base loss indices)  
677 represent pedochemical markers that do not show substantial modifications along strike and dip,  
678 and that exhibit consistent behaviour with depth across paleosol profiles. Translocation of Ca, with  
679 almost complete removal from the upper portions and concentration in lower horizons is a  
680 diagnostic feature of Po Plain paleosols. Some trace metal ratios experience significant variations  
681 across the weathering zones. Ba/Sr and Rb/Sr typically show a loss in the A horizons and gain in  
682 the Bk horizons, which is consistent with the identification of calcic horizons. On the other hand,  
683 redox-sensitive trace elements and Zr show increasing values from the parent material to upper  
684 paleosol horizons.

685

686

## 687 **Acknowledgments**

688

689 We are indebted to two anonymous reviewers, Guest Editors Giorgio Basilici and Augusto Varela,  
690 and Editor-in-Chief Thomas Algeo for their valuable and constructive comments and suggestions.

691

692 **References**

693

694 Aitken, J.F., Flint, S.S., 1996. Variable expressions of interfluvial sequence boundaries in the  
695 Breathitt Group (Pennsylvanian), eastern Kentucky, USA. Geological Society, London, Special  
696 Publications 104, 193–206.

697 Amorosi, A., Sammartino, I., 2018. Shifts in sediment provenance across a hierarchy of bounding  
698 surfaces: A sequence-stratigraphic perspective from bulk-sediment geochemistry.  
699 Sedimentary Geology 375, 145–156.

700 Amorosi, A., Centineo, M.C., Dinelli, E., Lucchini, F., Tateo, F., 2002. Geochemical and mineralogical  
701 variations as indicators of provenance changes in Late Quaternary deposits of SE Po Plain.  
702 Sedimentary Geology 151, 273–292.

703 Amorosi, A., Bruno, L., Rossi, V., Severi, P., Hajdas, I., 2014a. Paleosol architecture of a late  
704 Quaternary basin--margin sequence and its implications for high-resolution, non-marine  
705 sequence stratigraphy. Global and Planetary Change 112, 12–25.

706 Amorosi, A., Guermandi, M., Marchi, N., Sammartino, I., 2014b. Fingerprinting sedimentary and  
707 soil units by their natural metal contents: a new approach to assess metal contamination.  
708 Science of the total environment 500, 361–372.

709 Amorosi, A., Bruno, L., Campo, B., Morelli, A., 2015. The value of pocket penetration tests for the  
710 high-resolution palaeosol stratigraphy of late Quaternary deposits. Geological Journal 50,  
711 670–682.

712 Amorosi, A., Bruno, L., Campo, B., Morelli, A., Rossi, V., Scarponi, D., Hong, W., Bohacs, K.M.,  
713 Drexler, T.M., 2017a. Global sea-level control on local parasequence architecture from the  
714 Holocene record of the Po Plain, Italy. Marine and Petroleum Geology 87, 99–111.

715 Amorosi, A., Bruno, L., Cleveland, D.M., Morelli, A., Hong, W., 2017b. Paleosols and associated  
716 channel-belt sand bodies from a continuously subsiding late Quaternary system (Po Basin,  
717 Italy): New insights into continental sequence stratigraphy. Bulletin 129, 449–463.

718 Amorosi, A., Bruno, L., Campo, B., Costagli, B., Hong, W., Picotti, V., Vaiani, S.C., 2020. Deformation  
719 patterns of upper Quaternary strata and their relation to active tectonics, Po Basin, Italy.  
720 Sedimentology.

Anderson, J.B., Rodriguez, A., Abdulah, K.C., Fillon, R.H., Banfield L.A., McKeown, H.A., Wellner, J.S., 2004. Late Quaternary stratigraphic evolution of the northern Gulf of Mexico Margin: A synthesis. In: Anderson, J.B., Fillon, R.H. (Eds.), Late Quaternary Stratigraphic Evolution of the Northern Gulf of Mexico Margin. Society for Sedimentary Geology, Special Publication 79, 1–23.

Atchley, S.C., Nordt, L.C., Dworkin, S.I., 2004. Eustatic control on alluvial sequence stratigraphy: a possible example from the Cretaceous-Tertiary transition of the Tornillo Basin, Big Bend National Park, West Texas, USA. *Journal of Sedimentary Research* 74, 391–404.

Autin, W.J., Aslan, A., 2001. Alluvial pedogenesis in Pleistocene and Holocene Mississippi River deposits: Effects of relative sea-level change. *Geological Society of America Bulletin* 113, 1456–1466.

Bersezio, R., Giudici, M., Mele, M., 2007. Combining sedimentological and geophysical data for high-resolution 3-D mapping of fluvial architectural elements in the Quaternary Po Plain (Italy). *Sedimentary Geology* 202, 230–248.

Birkeland, P.W., 1999. *Soils and Geomorphology*, (3rd Ed.). Oxford University Press, New York. 448 pp.

Blum, M.D., Price, D.M., 1998. Quaternary alluvial plain construction in response to glacio-eustatic and climatic controls, Texas Gulf coastal plain. In: Shanley, K.W., McCabe, P.W. (Eds.), *Relative Role of Eustasy, Climate, and Tectonism in Continental Rocks: SEPM Special Publication* 59, 31–48.

Blum, M.D., Aslan, A., 2006. Signatures of climate vs. sea-level change within incised valley-fill successions: Quaternary examples from the Texas Gulf coast. *Sedimentary Geology* 190, 177–211.

Bruno, L., Amorosi, A., Severi, P., Costagli, B., 2017a. Late Quaternary aggradation rates and stratigraphic architecture of the southern Po Plain, Italy. *Basin Research* 29, 234–248.

Bruno, L., Bohacs, K.M., Campo, B., Drexler, T.M., Rossi, V., Sammartino, I., Scarponi, D., Hong, W., Amorosi, A., 2017b. Early Holocene transgressive palaeogeography in the Po coastal plain (northern Italy). *Sedimentology* 64, 1792–1816.

Bruno, L., Piccin, A., Sammartino, I., Amorosi, A., 2018. Decoupled geomorphic and sedimentary

750 response of Po River and its Alpine tributaries during the last glacial/post-glacial episode.  
751 *Geomorphology* 317, 184–198.

752 Bruno, L., Campo, B., Di Martino, A., Hong, W., Amorosi, A., 2019. Peat layer accumulation and  
753 post-burial deformation during the mid-late Holocene in the Po coastal plain (Northern Italy).  
754 *Basin Research* 31, 621–639.

755 Bruno, L., Marchi, M., Bertolini, I., Gottardi, G., Amorosi, A., 2020. Climate control on stacked  
756 paleosols in the Pleistocene of the Po Basin (northern Italy). *Journal of Quaternary Science* 35,  
757 559–571.

758 Busschers, F.S., Kasse, C., van Balen, R.T., Vandenberghe, J., Cohen, K.M., Weerts, H.J.T., Wallinga,  
759 J., Johns, C., Cleveringa, P., Bunnik, F.P.M., 2007. Late Pleistocene evolution of the Rhine–  
760 Meuse system in the southern North Sea basin: imprints of climate change, sea-level  
761 oscillation, and glacio-isostasy. *Quaternary Science Reviews* 26, 3216–3248.

762 Campo, B., Amorosi, A., Vaiani, S.C., 2017. Sequence stratigraphy and late Quaternary  
763 paleoenvironmental evolution of the Northern Adriatic coastal plain (Italy). *Palaeogeography,*  
764 *Palaeoclimatology, Palaeoecology* 466, 265–278.

765 Campo, B., Bohacs, K.M., Amorosi, A., 2020. Late Quaternary sequence stratigraphy as a tool for  
766 groundwater exploration: Lessons from the Po River Basin (northern Italy). *American*  
767 *Association of Petroleum Geologists Bulletin* 104, 681–710.

768 Castiglioni, G.B., 2001. Response of the fluvial system to environmental variations. In: Castiglioni,  
769 G.B., Pellegrini, G.B. (Eds.), *Illustrative Notes of the Geomorphological Map of Po Plain (Italy).*  
770 *Geografia Fisica Dinamica Quaternaria* 4, 165–188.

771 Chen, J., An, Z., Head, J., 1999. Variation of Rb/Sr ratios in the loess-paleosol sequences of Central  
772 China during the last 130,000 years and their implications for monsoon paleoclimatology.  
773 *Quaternary Research* 51, 215–219.

774 Chen, Q., Li, C., Li, P., Liu, B., Sun, H., 2008. Late Quaternary paleosols in the Yangtze Delta, China,  
775 and their paleoenvironmental implications. *Geomorphology* 100, 465–483.

776 Choi, K., Kim, J.H., 2006. Identifying late Quaternary coastal deposits in Kyonggi Bay, Korea, by  
777 their geotechnical properties. *Geo-Marine Letters* 26, 77–89.

778 Cleveland, D.M., Atchley, S.C., Nordt, L.C., 2007. Continental sequence stratigraphy of the Upper  
779 Triassic (Norian--Rhaetian) Chinle strata, northern New Mexico, USA: allocyclic and autocyclic  
780 origins of paleosol-bearing alluvial successions. *Journal of Sedimentary Research* 77, 909–924.

781 Cleveland, D.M., Nordt, L.C., Atchley, S.C., 2008. Paleosols, trace fossils, and precipitation  
782 estimates of the uppermost Triassic strata in northern New Mexico. *Palaeogeography,*  
783 *Palaeoclimatology, Palaeoecology* 257, 421–444.

784 Cremaschi, M., 1987. Paleosols and Vetusols in the Central Po Plain (Northern Italy): a study in  
785 Quaternary geology and soil development. Unicopli, Milan. 306 p.

786 Cremaschi, M., Nicosia, C., 2012. Sub-Boreal aggradation along the Apennine margin of the  
787 Central Po Plain: geomorphological and geoarchaeological aspects. *Géomorphologie: relief,*  
788 *processus, environnement* 2, 155–174.

789 Cremaschi, M., Fedoroff, N., Guerreschi, A., Huxtable, J., Colombi, N., Castelletti, L., Maspero, A.,  
790 1990. Sedimentary and pedological processes in the upper Pleistocene loess of Northern Italy.  
791 The Bagaggera sequence. *Quaternary International* 5, 23–38.

792 Dabrio, C.J., Zazo, C., Goy, J.L., Sierro, F.J., Borja, F., Lario, J., González, J.A., Flores, J.A., 2000.  
793 Depositional history of estuarine infill during the last postglacial transgression (Gulf of Cadiz,  
794 Southern Spain): *Marine Geology* 162, 381–404.

795 Dal' Bó, P.F., Basilici, G., Angelica, R.S., Bernardes Ladeira, F.S., 2009. Paleoclimatic interpretations  
796 from pedogenic calcretes in a Maastrichtian semi-arid eolian sand-sheet palaeoenvironment:  
797 Marília Formation (Bauru Basin, southeastern Brazil). *Cretaceous Research* 30, 659–675.

798 Delgado, L., Batezelli, A., Ladeira, F.S.B., Luna, J. 2019. Paleoenvironmental and paleoclimatic  
799 interpretation of the Late Cretaceous Marília Formation (Brazil) based on paleosol  
800 geochemistry. *Catena* 180, 365–382.

801 Demko, T.M., Currie, B.S., Nicoll, K.A., 2004. Regional paleoclimatic and stratigraphic implications  
802 of paleosols and fluvial/overbank architecture in the Morrison Formation (Upper Jurassic),  
803 Western Interior, USA. *Sedimentary Geology* 167, 115–135.

804 Driese, S.G., Ashley, G.M., 2016. Paleoenvironmental reconstruction of a paleosol catena, the Zinj  
805 archaeological level, Olduvai Gorge, Tanzania. *Quaternary Research* 85, 133–146.

806 Driese, S.G., Mora, C.I., Stiles, C.A., Joeckel, R.M., Nordt, L.C., 2000. Mass-balance reconstruction  
807 of a modern Vertisol: implications for interpreting the geochemistry and burial alteration of  
808 paleo-Vertisols. *Geoderma* 95, 179–204.

809 Fan, D., Shang, S., Burr, G., 2019. Sea level implications from late Quaternary/Holocene paleosols  
810 from the Oujiang delta, China. *Radiocarbon* 61, 83–99.

811 Franzini, M., Leoni, L., Saitta, M., 1972. A simple method to evaluate the matrix effects in X-ray  
812 fluorescence analysis. *X-ray Spectrometry* 1, 151–154.

813 Garcia, D., Joseph, P., Maréchal, B., Moutte, J., 2003. Patterns of geochemical variability in relation  
814 to turbidite facies in the Grès d'Annot Formation. In: P. Joseph, S.A. Lomas, Deep-Water  
815 Sedimentation in the Alpine Basin of SE France: New Perspectives on the Grès d'Annot and  
816 related systems. Geological Society London, Special Publications 221, 349–365.

817 Garzanti, E., Resentini, A., 2016. Provenance control on chemical indices of weathering (Taiwan  
818 river sands). *Sedimentary Geology* 336, 81–95.

819 Garzanti, E., Andò, S., 2019. Heavy minerals for junior woodchucks. *Minerals* 9, 148.

820 Garzanti, E., Padoan, M., Andò, S., Resentini, A., Vezzoli, G., Lustrino, M., 2013. Weathering and  
821 relative durability of detrital minerals in equatorial climate: sand petrology and geochemistry  
822 in the East African Rift. *The Journal of Geology* 121, 547–580.

823 Gibling, M.R., Bird, D.J., 1994. Late Carboniferous cyclothems and alluvial paleovalleys in the  
824 Sydney Basin, Nova Scotia: The Geological Society of America Bulletin 106, 105–117.

825 Gibling, M.R., Fielding, C.R., Sinha, R., Davidson, S.K., Leleu, S., North, C.P., 2011. Alluvial valleys  
826 and alluvial sequences: towards a geomorphic assessment. From River to Rock Record: The  
827 Preservation of Fluvial Sediments and Their Subsequent Interpretation: SEPM, Special  
828 Publication 97, 423–447.

829 Gile, L.H., Peterson, F.F., Grossman, R.B., 1965. The K horizon: a master soil horizon of carbonate  
830 accumulation. *Soil Science* 99, 74–82.

831 Gile, L.H., Peterson, F.F., Grossman, R.B., 1966. Morphological and genetic sequences of carbonate  
832 accumulation in desert soils. *Soil Science* 101, 347–360.

833 Harnois, L., 1988. The CIW index: a new chemical index of weathering. *SedG* 55, 319–322.



- 834 He, J., Garzanti, E., Dinis, P., Yang, S., Wang, H., 2020. Provenance versus weathering control on  
835 sediment composition in tropical monsoonal climate (South China) – 1. Geochemistry and  
836 clay mineralogy. *Chemical Geology* 558, 119860.
- 837 Hyland, E.G., Sheldon, N.D., 2016. Examining the spatial consistency of palaeosol proxies:  
838 Implications for palaeoclimatic and palaeoenvironmental reconstructions in terrestrial  
839 sedimentary basins. *Sedimentology* 63, 959–971.
- 840 Janssens, M.M., Kasse, C., Bohncke, S.J.P., Greaves, H., Cohen, K.M., Wallinga, J., Hoek, W.Z., 2012.  
841 Climate-driven fluvial development and valley abandonment at the last glacial-interglacial  
842 transition (Oude IJssel-Rhine, Germany). *Netherlands Journal of Geosciences* 91, 37–62.
- 843 Kahmann, J.A., Driese, S.G., 2008. Paleopedology and geochemistry of Late Mississippian  
844 (Chesterian) Pennington Formation paleosols at Pound Gap, Kentucky, USA: Implications for  
845 high-frequency climate variations. *Palaeogeography, Palaeoclimatology, Palaeoecology* 259,  
846 357–381.
- 847 Kasse, C., Bohncke, S.J.P., Vandenberghe, J., Gábris, G., 2010. Fluvial style changes during the last  
848 glacial–interglacial transition in the middle Tisza valley (Hungary): Proceedings of the  
849 Geologists’ Association 121, 180–194.
- 850 Kraus, M.J., 2002. Basin-scale changes in floodplain paleosols: implications for interpreting alluvial  
851 architecture. *Journal of Sedimentary Research* 72, 500–509.
- 852 Kvale, E.P., Archer, A.W., 2007. Paleovalley fills: Trunk vs. tributary. *American Association of*  
853 *Petroleum Geologists Bulletin* 91, 809–821.
- 854 Leoni, L., Saitta, M., 1976. Determination of yttrium and niobium on standard silicate rocks by X-  
855 ray fluorescence analyses. *X-ray Spectrometry* 5, 29–30.
- 856 Leoni, L., Menichini, M., Saitta, M., 1982. Determination of S, Cl and F in silicate rocks by X-Ray  
857 fluorescence analyses. *X-Ray Spectrometry* 11, 156–158.
- 858 Machette, M.N., 1985. Calcific soils of the southwestern United States. *Soils and Quaternary*  
859 *geology of the southwestern United States: Geological Society of America Special Paper* 203,  
860 1–21.
- 861 Marriott, S.B., Wright, V.P., 1993. Palaeosols as indicators of geomorphic stability in two Old Red

862 Sandstone alluvial suites, South Wales. *Journal of the Geological Society* 150, 1109–1120.

863 Maynard, J.B., 1992. Chemistry of modern soils as a guide to interpreting Precambrian paleosols.  
864 *The Journal of Geology* 100, 279–289.

865 McCarthy, P.J., Plint, A.G., 1998. Recognition of interfluvial sequence boundaries: integrating  
866 paleopedology and sequence stratigraphy. *Geology* 26, 387–390.

867 McCarthy, P.J., Plint, A.G., 2003. Spatial variability of palaeosols across Cretaceous interfluvial  
868 the Dunvegan Formation, NE British Columbia, Canada: palaeohydrological,  
869 palaeogeomorphological and stratigraphic implications. *Sedimentology* 50, 1187–1220.

870 McCarthy, P.J., Plint, A.G., 2013. A pedostratigraphic approach to nonmarine sequence  
871 stratigraphy: a three-dimensional paleosol-landscape model from the Cretaceous  
872 (Cenomanian) Dunvegan Formation, Alberta and British Columbia, Canada. In: Driese, S.G.,  
873 Nordt, L.C. (Eds.), *New Frontiers in Paleopedology and Terrestrial Paleoclimatology: Paleosols  
874 and Soil Surface Analog Systems: Society for Sedimentary Geology Special Publication 104*,  
875 159–177.

876 McFadden, L.D., Tinsley, J.C., 1985. Rate and depth of pedogenic-carbonate accumulation in soils:  
877 formulation and testing of a compartment model, in: *Soils and Quaternary Geology of the  
878 Southwestern United States*. Geological Society of America, pp. 23–41.

879 McFadden, L.D., Amundson, R.G., Chadwick, O.A., 1991. Numerical Modeling Chemical, and  
880 Isotopic Studies of Carbonate Accumulation in of Arid Regions. Occurrence, characteristics,  
881 and genesis of carbonate, gypsum, and silica accumulations in soils 26, 17–35.

882 McFadden, L.D., McDonald, E. V, Wells, S.G., Anderson, K., Quade, J., Forman, S.L., 1998. The  
883 vesicular layer and carbonate collars of desert soils and pavements: formation, age and  
884 relation to climate change. *Geomorphology* 24, 101–145.

885 Mohanty, S.P., Nanda, S., 2016. Geochemistry of a paleosol horizon at the base of the Sausar  
886 Group, central India: Implications on atmospheric conditions at the Archean--  
887 Paleoproterozoic boundary. *Geoscience Frontiers* 7, 759–773.

888 Mol, J., 1997. Fluvial response to Weichselian climate changes in the Niederlausitz (Germany).  
889 *Journal of Quaternary Science: Published for the Quaternary Research Association* 12, 43–60.

890 Mongrain, J.R., McCarthy, P.J., Plint, A.G., Fowell, S.J., 2013. Integrated paleopedology and  
891 palynology from alluvial paleosols of the Cretaceous (Cenomanian) Dunvegan Formation,  
892 Alberta and British Columbia, Canada: paleoenvironmental and stratigraphic implications. In:  
893 Driese, S.G., Nordt, L.C. (Eds.), *New Frontiers in Paleopedology and Terrestrial*  
894 *Paleoclimatology: Paleosols and Soil Surface Analog Systems*: Society for Sedimentary  
895 *Geology Special Publication 104*, 231–255.

896 Mora, C.I. and Driese, S.G., 1999. Paleoenvironment, paleoclimate and stable carbon isotopes of  
897 Paleozoic red-beds palaeosols, Appalachian Basin, U.S.A. and Canada. In: Thiry, M. and  
898 Coincon, R.S. (Eds.), *Palaeoweathering, Palaeosurfaces, and Related Continental Deposits*:  
899 *International Association of Sedimentologists, Special Publication 27*, 61–84.

900 Morelli, A., Bruno, L., Cleveland, D.M., Drexler, T.M., Amorosi, A., 2017. Reconstructing Last Glacial  
901 Maximum and Younger Dryas paleolandscapes through subsurface paleosol stratigraphy: An  
902 example from the Po coastal plain, Italy. *Geomorphology* 295, 790–800.

903 Nesbitt, H.W., Young, G.M., 1982. Early Proterozoic climates and plate motions inferred from  
904 major element chemistry of lutites. *nature* 299, 715–717.

905 Nesbitt, H.W., Young, G.M., McLennan, S.M., Keays, R.R., 1996. Effects of chemical weathering and  
906 sorting on the petrogenesis of siliciclastic sediments, with implications for provenance  
907 studies. *The Journal of Geology* 104, 525–542.

908 Plint, A.G., McCarthy, P.J., Faccini, U.F., 2001. Nonmarine sequence stratigraphy: updip expression  
909 of sequence boundaries and systems tracts in a high-resolution framework, Cenomanian  
910 Dunvegan Formation, Alberta foreland basin, Canada. *AAPG bulletin* 85, 1967–2001.

911 Price, J.R., Velbel, M.A., 2003. Chemical weathering indices applied to weathering profiles  
912 developed on heterogeneous felsic metamorphic parent rocks. *Chemical Geology* 202, 397–  
913 416.

914 Prochnow, S.J., Nordt, L.C., Atchley, S.C., Hudec, M.R., 2006. Multi-proxy paleosol evidence for  
915 middle and late Triassic climate trends in eastern Utah. *Palaeogeography, Palaeoclimatology,*  
916 *Palaeoecology* 232, 53–72.

917 Reigemborn, M.S., Beilinson, E., 2020. Stratigraphic architecture and paleosols as basin correlation  
918 tools of the early Paleogene infill in central–south Patagonia, Golfo San Jorge Basin,

919 Argentinean Patagonia. *J. S. Am. Earth Sci.* 99, 102519.

920 Retallack, G.J., 1988. Field Recognition of Paleosols. *GSA Sp. Paper*, pp. 1–20.

921 Retallack, G.J., 1997a. Early forest soils and their role in Devonian global change. *Science* 276, 583–  
922 585.

923 Retallack, G.J., 1997b. Neogene expansion of the North American prairie. *Palaios* 12, 380–390.

924 Retallack, G.J., 1997c. Palaeosols in the upper Narrabeen Group of New South Wales as evidence  
925 of Early Triassic palaeoenvironments without modern analogues. *Australian Journal of Earth*  
926 *Sciences* 44, 185–201.

927 Retallack, G.J., 1999. Post-apocalyptic greenhouse paleoclimate revealed by earliest Triassic  
928 paleosols in the Sydney Basin, Australia. *Geological Society of America Bulletin* 111, 52–70.

929 Retallack, G.J., 2001a. *Soils of the Past: an Introduction to Paleopedology*, 2nd Rev., Blackwell  
930 Publishing, Oxford. 404 p.

931 Retallack, G.J., 2001b. Cenozoic expansion of grasslands and climatic cooling. *The Journal of*  
932 *Geology* 109, 407–426.

933 Retallack, G.J., 2007. Soils and global change in the carbon cycle over geological time. In: Holland,  
934 H.D., Turekian, K.K. (Eds.), *Treatise on geochemistry*, v. 5. Pergamon Press, Oxford, pp. 581–  
935 605.

936 Retallack, G.J., Bestland, E.A., Fremd, T., 2000. Eocene and Oligocene paleosols and environmental  
937 change in central Oregon. *Geological Society of America Special Paper* 344, 192 pp.

938 Ruxton, B.P., 1968. Measures of the degree of chemical weathering of rocks. *The Journal of*  
939 *Geology* 76, 518–527.

940 Shanley, K.W., McCabe, P.J., 1994. Perspectives on the sequence stratigraphy of continental strata.  
941 *American Association of Petroleum Geologists Bulletin* 78, 544–568.

942 Shao, J.Q., Yang, S.Y., 2012. Does chemical index of alteration (CIA) reflect silicate weathering and  
943 monsoonal climate in the Changjiang River basin? *Chinese Science Bulletin* 57, 1178–1187.

944 Scarciglia, F., Mercatante, G., Fonddevilla, V., Anadón, P., Oms, O., Donato, P., Agnini, C., Papini, M.,  
945 Rook, L., Ghinassi, M., 2018. Pleistocene paleosol development and paleoenvironmental

946 dynamics in East Africa: A multiproxy record from the Homo-bearing Aalat pedostratigraphic  
947 succession, Dandiero basin (Eritrea). *Quaternary Science Reviews* 191, 275–298.

948 Schwertmann, U., 1993. Relations between iron oxides, soil color, and soil formation. *Soil color* 31,  
949 51–69.

950 Sheldon, N.D., Tabor, N.J., 2009. Quantitative paleoenvironmental and paleoclimatic  
951 reconstruction using paleosols. *Earth-Science Reviews* 95, 1–52.

952 Sinha, R., Kumar, R., Sinha, S., Tandon, S.K., Gibling, M.R., 2007. Late Cenozoic fluvial successions  
953 in northern and western India: an overview and synthesis. *Quaternary Science Reviews* 26,  
954 2801–2822.

955 Soil Survey Staff., 1999. *Soil Taxonomy. A basic system of soil classification for making and*  
956 *interpreting soil surveys, Agricultural Handbook. Natural Resources Conservation Service,*  
957 *USDA: Washington, DC. 436.*

958 Sprague, R.A., Melvin, J.A., Conradi, F.G., Pearce, T.J., Dix, M.A., Hill, S.D., Canham, H., 2009.  
959 Integration of core-based chemostratigraphy and petrography of the Devonian Jauf  
960 sandstones. In: Uthmaniyah Area, Ghawar Field, Eastern Saudi Arabia. *AAPG Search and*  
961 *Discovery Article* 20065, pp. 34.

962 Srivastava, P., Rajak, M.K., Sinha, R., Pal, D.K., Bhattacharyya, T., 2010. A high-resolution  
963 micromorphological record of the Late Quaternary paleosols from Ganga-Yamuna interfluvium:  
964 stratigraphic and paleoclimatic implications: *Quaternary International*, v. 227, no. 2, p. 127–  
965 142.

966 Srivastava, P., Sinha, R., Deep, V., Singh, A., Upreti, N., 2018. Micromorphology and sequence  
967 stratigraphy of the interfluvium paleosols from the Ganga Plains: a record of alluvial cyclicity and  
968 paleoclimate during the Late Quaternary. *Journal of Sedimentary Research* 88, 105–128.

969 Tandon, S.K., Gibling, M.R., 1997. Calcretes at sequence boundaries in Upper Carboniferous  
970 cyclothems of the Sydney Basin, Atlantic Canada. *Sedimentary Geology* 112, 43–67.

971 Tentori, D., Amorosi, A., Milli, S., Marsaglia, K.M., 2021. Sediment dispersal pathways in the Po  
972 coastal plain since the Last Glacial Maximum: provenance signals of autogenic and eustatic  
973 forcing. *Basin Research* 33, 1407–1428.

974 van Balen, R.T., Busschers, F.S., Tucker, G.E., 2010. Modeling the response of the Rhine--Meuse  
975 fluvial system to Late Pleistocene climate change. *Geomorphology* 114, 440–452.

976 Van Wagoner, J.C., Mitchum, R.M., Campion, K.M., Rahmanian, V.D., 1990. Siliciclastic sequence  
977 stratigraphy in well logs, cores, and outcrops: concepts for high-resolution correlation of time  
978 and facies. *American Association of Petroleum Geologists, Methods in Exploration 7: Tulsa,*  
979 *U.S.A, 55 p.*

980 Varela, A.N., Raigemborn, M.S., Richiano, S., White, T., Poiré, D.G. Lizzoli, S., 2018. Late Cretaceous  
981 paleosols as paleoclimate proxies of high-latitude Southern Hemisphere: Mata Amarilla  
982 Formation, Patagonia, Argentina. *Sedimentary Geology* 363, 83–95.

983 Vinogradov, A.P., 1959. Geochemistry of isotopes. *International Geology Review* 1, 1–13.

984 Xu, Z., Liu, C.-Q., 2010. Water geochemistry of the Xijiang basin rivers, South China: Chemical  
985 weathering and CO<sub>2</sub> consumption. *Applied Geochemistry* 25, 1603–1614.

986 Zuffetti, C., Trombino, L., Zembo, I., Bersezio, R., 2018. Soil evolution and origin of landscape in a  
987 late Quaternary tectonically mobile setting: The Po Plain-Northern Apennines setting in  
988 Lombardy (Italy). *Catena* 171, 376–397.

989

990

991 Supplementary Table 1. Location and elevation of the 17 cores studied for geochemical analysis.

992 Supplementary Table 2. XRF geochemistry (major and trace element analysis) of the study  
993 paleosols.